School of Engineering and Physical Sciences
-
Department of Electronic Electrical and Computing Engineering

School of Engineering
-
Department of Mechanical Engineering

FABRICATION OF 2D MATERIAL BASED RESONATORS

An Hoang Tran

MASTER OF SCIENCE DISSERTATION

EPFL Supervisors: Dr. Tom Larsen, Prof. Guillermo Villanueva
HWU Supervisor: Dr. Changhai Wang

Lausanne, 03 July 2017

Declaration

I, Tran Hoang An, confirm that this dissertation, titled “Fabrication of 2D Material Based Resonators”, is submitted for assessment of the master’s thesis of the programme Erasmus Mundus Master in Smart Systems Integration run collaboratively by Herriot-Watt University (Scotland), University College of Southeast Norway (Norway) and Budapest University of Technology and Economics (Hungary). This work was conducted in an exchange Master project at the École polytechnique fédérale de Lausanne (EPFL) in Switzerland.

I declare that this is my own work which was written based on my own understanding and investigation. Any uses made within it of the works of other authors in any form (e.g. ideas, equations, figures, text, tables, codes) are properly acknowledged at the point of their use. All references used in this work have been mentioned completely with full bibliography.

Signed: **An H. Tran**

Date: 03/07/2017

Acknowledgements

First, I would like to express my sincerest thanks to Dr. Tom Larsen and Prof. Guillermo Villanueva for their support and guidance throughout the duration of this project. Without their sharp technical advice, this work would not have been possible. Especially, I owe my immense gratitude to Dr. Tom Larsen for his ingenious instructions on how to use several tools and equipment in the clean room and the lab and his clever views on why things go wrong.

Secondly, I would like to thank all the amazing people in the ANEMS group who have made my stay here cheerful and enjoyable. Last but not the least, I am deeply grateful to my family in Vietnam for their encouragement and unwavering support throughout the duration of my master dissertation.

Abstract

Improvements in manufacturing processes inspired by the semiconductor integrated circuit industry have seen a sharp reduction in dimensions of microelectromechanical systems (MEMS), leading to the emergence of its submicron counterpart – nanoelectromechanical systems (NEMS). NEMS resonators, nano-scale vibrating structures, have proven to be extremely sensitive sensors of physical phenomena which affect its resonance behaviour. The arrival of graphene and other 2D materials with ultrahigh surface to volume ratio, ultralow mass and a diverse range of superior electrical and mechanical properties marked an important moment in NEMS resonators' history as the reality of having extremely sensitive NEMS resonator based sensors seems imminent. Although a fair amount of research has demonstrated the potential of 2D materials for NEMS resonators, the employed fabrication methods either are not scalable or involve too many fabrication steps.

An efficient and mass-reproducible fabrication process for 2D material based NEMS resonators has been successfully demonstrated. This fabrication method is predicted to be compatible with any 2D materials although graphene was chosen for availability and cost purposes. Metal electrodes for electrostatic actuation and detection are lithographically patterned on a silicon wafer with wet thermal oxide which was then diced into small substrates to host graphene. Graphene was transferred using a wet-transfer method on these electrode chips before being optimally patterned with photolithography and oxygen plasma etch. Free-standing graphene beams were obtained by wet etching the underlying oxide and critical point drying. Compared to the existing large-scale fabrication methods of 2D material based NEMS resonators, suspended graphene is clamped on top of metal electrodes fabricated on the wafer level, resulting in a smaller number of fabrication steps and minimal exposure of graphene to sacrificial layers. The fabricated devices were electrically characterised and the graphene's sheet resistances were derived and benchmarked against those found in literature. The characteristic bipolar field effect transistor (FET) behaviour of graphene was confirmed. The generic fabrication approach demonstrated in this thesis holds great promise for 2D material based resonators being fabricated with high reproducibility and scalability.

Keywords: Nanoelectromechancial Systems (NEMS), resonators, 2D materials, graphene, sensor, fabrication

TABLE OF CONTENTS

List of Figures and Tables

Chapter 1

Introduction

1.1 Background about M/NEMS Resonators

MicroElectroMechanical Systems (MEMS) are micro-scale systems that incorporate electrical and mechanical elements to perform certain functions. MEMS devices have dimensions in the range of a few to hundreds of microns and are characterised by the ability to sense, control and actuate on the micro scale, generating effect at the macro scale [1]. A typical MEMS device often contains movable mechanical microstructures that can microscopically move upon interaction with a physical stimulus to be sensed, or can be actuated to perform a function. The electrical elements process information obtained from the sensing and control the actuation of the microstructures. The well-established fabrication approaches from in the semiconductor integrated circuit (IC) manufacturing, such as lithography, thin film deposition and etching, have boosted the growth of MEMS and turned it into a largely mature industry [2]. Some well-known MEMS commercial products include accelerometers (for automotive airbag sensors), gyroscopes (for orientation determination in vehicles, smartphones, games consoles, etc.), inkjet printer nozzles, microphones, video projector display chips, blood pressure sensor, and many others. Recent advancements in manufacturing technologies and the developments of new materials have enabled the scaling down of MEMS to the sub-micron domain. These sub-micron MEMS, with at least one dimension smaller than 1 μm, have been termed NanoElectroMechanical Systems (NEMS) [3]. This regime brings a new promise for unprecedentedly sensitive sensors, minimally invasive medical diagnostics and ultra-high data storage. MEMS and their extension NEMS are hereinafter referred to as “M/NEMS”.

Resonators are mechanical systems that exhibit the resonance behaviour in which their vibration occurs with greater amplitudes at certain frequencies than others. These frequencies are called the natural frequencies or resonant frequencies. M/NEMS resonators are miniaturised mechanical resonators consisting of free-standing or suspended micro- or nano-structures that oscillate at high frequencies. M/NEMS resonators with small sizes and new properties have revolutionised many sensor applications with extremely high sensitivity to

charge, mass, force, temperature, etc. [4]. The sensing principle of M/NEMS resonators lies in the effect that physical stimuli (i.e., measurands) have on the oscillation of the resonators. The change in resonant frequency, vibration amplitude, phase or damping can be quantified and correlated back to the stimuli [5]. Figure 1.1 summarises different physical quantities that can be detected by resonator-based sensors and the intermediate signals that are picked up by the resonator.

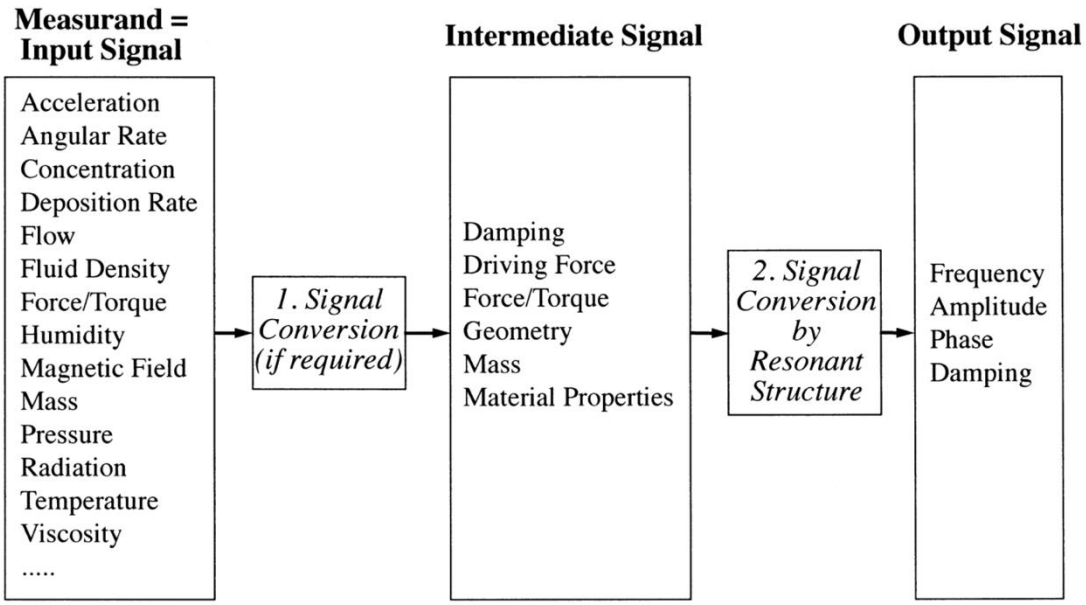

Figure 1.1: Different physical quantities that can be probed by a resonator and the intermediate signals that directly affect its oscillation [5].

A resonator's resonance is directly determined by its geometry, dimensions, stiffness and mass density [6]. Sub-micron dimensions and low mass in NEMS resonators endow them with very high mechanical responsivity which translates to sensors having extremely high sensitivity and operating at ultralow power. Reduced dimensions also correspond to an increase in the resonator's resonant frequency leading to extremely fast and robust devices. Table 1 presents the obtainable resonant frequencies for suspended beam resonators with dimensions going from MEMS to NEMS, and with Silicon Carbide (SiC), Silicon (Si), and Gallium Arsenide (GaAs) as structural materials. The resonant frequencies are drastically dependent upon the geometries and dimensions of the resonators. It is noted that for the same dimensions and geometry, the resonator's resonant frequency is significantly higher for materials with higher stiffness (Young's moduli of SiC, Si, GaAs are 450 GPa, 179 GPa and 85 GPa, respectively).

Table 1: Resonant frequencies of various M/NEMS resonators with different geometries, dimensions and structural materials being SiC [Si] (GaAs) [3].

Resonator geometries	**Resonator dimensions (length × width × thickness, in μm)**			
	100 × 3 × 0.1	*10 × 0.2 × 0.1*	*1 × 0.05 × 0.05*	*0.1 × 0.01 × 0.01*
Both ends clamped 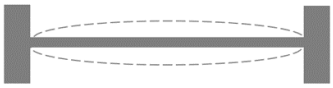	*120 KHz* *[77]* *(42)*	*12 MHz* *[7.7]* *(4.2)*	*590 MHz* *[380]* *(205)*	*12 GHz* *[7.7]* *(4.2)*
Both ends pinned 	*53 KHz* *[34]* *(18)*	*5.3 MHz* *[3.4]* *(1.8)*	*260 MHz* *[170]* *(92)*	*5.3 GHz* *[3.4]* *(1.8)*
Cantilever 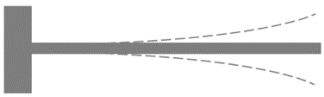	*19 KHz* *[12]* *(6.5)*	*1.9 MHz* *[1.2]* *(0.65)*	*93 KHz* *[60]* *(32)*	*1.9 GHz* *[1.2]* *(0.65)*

1.2 Two-dimensional (2D) Materials and their potential use in NEMS

This section aims to give an introduction about 2D materials and provide the rationale for why they are appealing candidates for NEMS resonators. An overview of graphene and other 2D materials with strong emphasis on their most notable properties is presented before the main attributes that make them attractive for NEMS resonators are discussed.

1.2.1 2D Materials and their properties

2D materials are a class of nanomaterials that are one or a few atoms thick. They are commonly obtained from exfoliating layered materials consisting of atomic sheets weakly bonded by van der Waals interaction. The first 2D material to be isolated and probably the most well-known is graphene [7]. Graphene is a 2D atomically thick allotrope of carbon which consists of carbon atoms arranged in a hexagonal lattice, with each atom located at each vertex. Each carbon atom in the lattice is connected to each of the three neighbouring atoms via one sigma (σ) bond formed by overlapping two sp^2 orbitals while the remaining un-hybridised sp^2 orbital is oriented out of plane [8]. Graphene is fundamentally the building blocks of all graphitic materials of all dimensionalities such as graphite, carbon nanotube and fullerenes (Figure 1.2) [9].

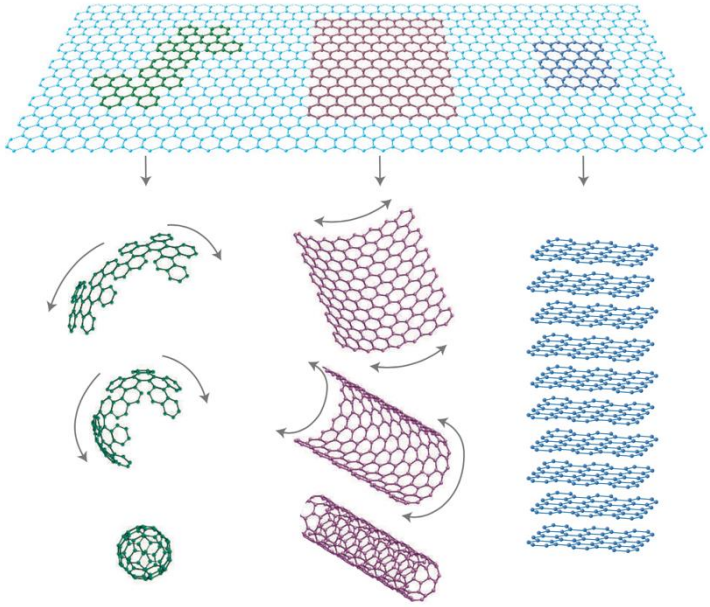

Figure 1.2: Graphene is essentially the structural elements of all graphitic carbon allotropes of different dimensionalities. It can be wrapped up into zero-dimensional (0D) fullerene, rolled into one-dimensional (1D) carbon nanotube or stacked into graphite [9].

Since its discovery in 2004, graphene has attracted an enormous amount of interest from scientific communities due to its superior electronic, mechanical, thermal and optical properties. Graphene possesses a unique band structure which consists of valence bands and conduction bands touching at single points called the Dirac points. Since the energy-momentum dispersion relation is linear near the Dirac points, the electrons and holes behave like relativistic particles with zero effective mass and with an energy-independent Fermi velocity that is 300 times smaller than the speed of light [10]. The massless behaviour and high Fermi velocity make graphene an extremely good conductor of electricity. The intrinsic limit of graphene's electron mobility is 200,000 $cm^2\ V^{-1}\ s^{-1}$ at room temperature, higher than any known materials [11]. Due to the strength of the planar sigma (σ) bonds, graphene is the strongest material ever discovered, about 200 times stronger than structural steel [12]. The two-dimensional elastic stiffness of graphene is 340 newtons per metre (N/m), corresponding to a Young's modulus of 1 tera-pascals (TP). The graphene's intrinsic breaking strength is 42 N/m. Graphene can be extended to a critical breaking strain of 25% without causing any damage. Graphene's thermal properties are equally impressive. Its room temperature (RT) thermal conductivity has been reported to be as high as 5000 watts per milli-kevins (W/mK), about ten times higher than that of copper [13]. Graphene also possesses unique optical properties. Despite being only one-atom thick, graphene's optical absorption is 2.3% in the visible spectrum and it can be optically visualised [14]. Being a semimetal with zero bandgap,

graphene can absorb a wide range of wavelengths of light, with the relatively flat absorption spectrum covering the entire ultraviolet-far infrared range [14] [15].

More than a decade since the successful isolation of graphene, many other 2D materials with more versatility than graphene, including insulators (e.g., Hexagonal Boron Nitride nano-sheets), conductors (e.g., Borophene) and semiconductors (e.g., Phosphorene, Molybdenum Disulfide), have been uncovered. These 2D materials have unique physical properties that are complementary to those in graphene. In the next paragraphs, some frequently used and technologically important 2D materials "beyond graphene" are discussed.

The hexagonal Boron Nitride nano-sheets (h-BN) are single- or few- layer 2D materials exfoliated from bulk h-BN, much in the same way graphene can be acquired by exfoliating graphite. Like graphene, h-BN's lattice consists of sp^2 conjugated boron and nitrogen atoms forming a honeycomb structure. However, unlike graphene, the two atoms of nitrogen (N) and Boron (B) in a h-BN unit cell exhibit different on-site energies, leading to a large bandgap (5.97 eV) [16]. h-BN is therefore a good insulator. h-BN also possesses high thermal conductivity, high mechanical stiffness and low mass density, with RT thermal conductivity of 600 W/mK, Young's modulus of 810 GPa and mass density of 2.1 g/cm^3 [17].

Another set of 2D materials that have gained significant attention over the past few years are Transition Metal Dichalcogenide monolayers (TMDCs). Just like graphite and bulk h-BN, bulk TMDCs are layered materials with strong in-plane bonding and weak out-of-plane interaction that allow exfoliation into TMDCs of one unit cell thickness [18]. The most frequently used TMDCs, such as Molybdenum Disulfide (MoS_2), Molybdenum diselenide ($MoSe_2$), Tungsten disulfide (MoS_2) and Tungsten diselenide (WS_2), are semiconductors having tunable bandgaps that shift from indirect to direct when going from bulk to monolayer [19]. Among the 2D TMDCs, MoS_2 has been shown to have excellent mechanical properties similar to those of graphene. These properties include ultralow weight (monolayer mass density of 3.3 $fg/\mu m^2$ for MoS_2), high breaking strain (10-20% for MoS_2) and high stiffness (Young's modulus of 200-300 GPa for MoS_2) [20] [21] [22].

Phosphorene, the 2D form of black phosphorous, is another 2D material that has recently been brought under the spot light. Much like the previously discussed 2D materials, phosphorene is the single layer building block of the layered bulk black phosphorous, which can be formed by stacking multiple layers of phosphorene on top of each other. Phosphorene has a distinct lattice structure where the phosphorous atoms are arranged laterally in an "puckered/corrugated" manner (Figure 1.3a). The interesting electronic property of phosphorene is that it is a semiconductor with a thickness-dependent bandgap from 0.33 eV

(bulk) to 1.5 eV (monolayer) and a good carrier mobility of up to ~1,000 $cm^2V^{-1}s^{-1}$ [23]. Monolayer phosphorene can sustain a tensile strain of up to 27% and 30% in the two in-plane directions [24]. Due to the corrugated arrangement of atoms their lattice, phosphorene possess highly directional elastic stiffness (Young's modulus of 37 - 41.3 GPa and 106.4 - 159 GPa in the two in-plane directions) [24] [25].

Many other 2D materials exist and display distinct electronic, mechanical and transport properties. An in-depth discussion of these materials is beyond the scope of this section. Ref. [26] provides a detailed report on 2D materials beyond graphene. Finally, it has been demonstrated that mixing and matching these 2D materials with each other or with common 1D and 3D materials result readily in novel van der Waals heterostructures (vdWHs) with specific characteristics [19]. Figure 1.3 shows the lattice structures of some commonly used 2D materials and how new vdWHs can be formed by combining these 2D materials with each other or with other dimensional materials.

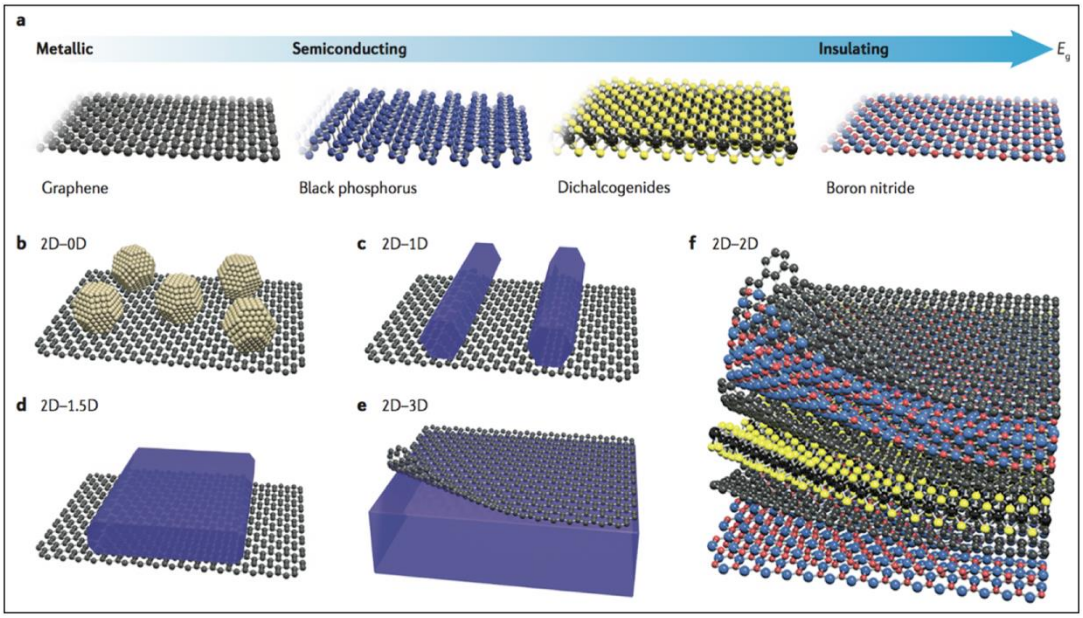

Figure 1.3: 2D materials and van der Waals heterostructures (vdWHs). (a) A wide variety of 2D materials are available with different chemical compositions and lattice structures, rendering them metallic, semiconducting or insulating, (b)-(f) vdWHs formed by combining 2D materials with 0D particles or quantum dots, 1D nanowires, 1.5D nanoribbons, 3D bulk materials or other 2D nanosheets [19].

The exciting properties of 2D materials that are very different from their bulk counterparts have opened possibilities for a multitude of applications such as field effect transistor (FET) [27] [28], solar cells [29] [30], flexible organic light emitting diode (OLED) [31], molecular gas sensors [32], supercapacitors [33] and DNA sequencing [34].

1.2.2 Potential use of 2D Material for NEMS Resonators

2D materials appear the perfect match for NEMS resonators. The most important attribute that sets 2D materials apart from conventional 3D and 1D materials in making ultrasensitive resonator-based sensors is the fact that they are only one or a few atoms thick thus possessing an extremely large surface to volume ratio. This makes 2D material based resonators very responsive as the external stimulus at the material's surface greatly alters its mass density. 2D materials also offer outstanding mechanical properties with high stiffness and breaking strain. As discussed in the previous section, the Young's moduli of graphene, MoS_2 and h-BN are 1TPa, 810 GPa and 300 GPa, respectively, and are larger than those of silicon (180 GPa) and silicon nitride (300 GPa), the most popular structural materials for high performance M/NEMS. 2D materials' ultralow mass and high stiffness ensure resonators based on these materials operate at ultrahigh frequencies and ultimate resonant frequencies in the THz range can potentially be reached [3]. 2D materials' high breaking strains suggests the possibility of strain engineering. New resonator based sensor's read-out schemes can be achieved where the resonator's resonance is probed by monitoring the shift in the strain-dependent optical absorption or photoluminescence [35].

Another interesting feature of 2D materials is the fact that their properties can be easily tuned. For example, the fact that graphene optical absorption can be modulated by applying a nearby electric field implies the potential realisation of novel graphene-based infrared detectors [36]. 2D materials come in great diversity. The list of 2D materials have constantly grown since the discovery of graphene, adding to the already abundant catalogue of 2D materials that have distinctly interesting physical properties. This diversity and the possibility to combine different 2D materials with each other and with other nanostructures to realise novel device characteristics hold promise for high performance 2D material based resonators in a wide range of sensing applications.

Finally, 2D materials presents a good prospect of effective fabrication methods for NEMS resonators. Most works on Si-based NEMS resonators implement a "top-down" fabrication approach that starts from bulk silicon and obtains resonating released structures by successive lithography and etching process steps. Recent years have seen the "bottom-up" fabrication approach gaining increased attention as NEMS resonators utilise nano-structures such as nanowires and nanotubes as building blocks [37] [38]. 2D materials offer the possibility of combining the advantages of both top down and bottom up fabrication approaches since they are intrinsically nano-scale and yet can be lithographically manipulated [39].

1.3 Thesis Objective and Structure

1.3.1 Thesis Objective

The main objective of this thesis is to implement a mass-reproducible and efficient fabrication procedure for 2D material based NEMS resonators. The fabrication approach should feature an efficient transfer of 2D materials films obtained from a scalable production method and comprise a minimal number of fabrication steps while still maintaining a good quality of 2D materials in the fabricated resonators.

Several high-profile research achievements on 2D material based resonators are available and demonstrative of 2D materials' potential to be used in high performance NEMS resonators. The ultimate purpose is to achieve suspended resonating 2D material based structures. The first study on 2D material based resonator was carried out with graphene being exfoliated over trenches etched in silicon oxide (SiO_2) [40]. Other works on resonators from other 2D materials also obtain suspended structures by exfoliating and transferring MoS_2 and h-BN on pre-patterned trenches [41] [42]. While these fabrication approaches provide a reliable route towards the demonstration of proof-of-concept devices and for fundamental studies, they are hardly mass-reproducible. This is because it is not possible to exfoliate 2D materials in large sheets with good control of the number of layers, shapes and positions of the film [43]. Some other attempts to make 2D material suspended structures on large scales employ 2D materials grown by chemical vapour deposition (CVD) and various transfer and lithography steps to pattern graphene together with metal electrodes for subsequent actuation and detection. [44] [45]. However, the drawbacks of the fabrication methods implemented in these studies are the extensive exposure of 2D materials to different sacrificial layers such as photoresist and numerous sophisticated fabrication steps involved on small substrates. This is partly due to fact that the suspended 2D materials employed in these resonators are placed under the metal electrodes that are used for electrical actuation.

This thesis aims to demonstrate a simple, cost-effective and high-yield fabrication approach for 2D material based resonators where most fabrication steps are carried out on the wafer scale. Suspended 2D material are placed on top of metal electrodes and good graphene-metal clamping is ensured through van der Waal forces. Graphene is chosen as the 2D material for fabricating the resonator in this project as it is cheap, well-studied and readily available. However, it is important to recognise that the employed fabrication strategy should be compatible and applicable to any other 2D materials.

1.3.2 Thesis Structure

The thesis is organised in the following structure:

- **Chapter 1**: *Introduction*

  A brief introduction about MicroElectroMechanical Systems (MEMS), NanoElectroMechanical Systems (NEMS) and M/NEMS resonators are presented before an overview of 2D materials and their potential for NEMS resonators is explained. The chapter concludes with the thesis motivation and structure.

- **Chapter 2**: *Graphene based NEMS resonators*

  This chapter begins with an overview of graphene production methods. Then a literature review about graphene based NEMS resonators is presented with focus on the fabrication and transduction techniques. Finally, a discussion on the design schematics and working principles of the graphene based NEMS resonator employed in this thesis is given.

- **Chapter 3**: *Graphene transfer and device fabrication*

  In the first part of this chapter, a brief discussion about graphene transfer processes is delivered before the employed graphene transfer procedures are described. The second part of the chapter is dedicated to discussing the device fabrication approach employed in this thesis including the process flow and mask design. Finally, the encountered issues during fabrication, their solutions and a summary of the fabrication results are provided.

- **Chapter 4**: *Device characterisation*

  Details about how the device's metal-contact resistivity and graphene sheet resistance of the unsuspended and suspended graphene are measured and characterised are specified. The measurement results of graphene's transport properties are discussed.

- **Chapter 5**: *Conclusion and future works*

  A discussion about what have been achieved in the thesis followed by an outlook on the future works is given.

Chapter 2

Graphene-based NEMS Resonators

This chapter aims to give an overview of graphene-based NEMS (GNEMS) resonators. Special focus will be placed on the fabrication techniques as well as actuation and detection methods for GNEMS resonators after a brief review of common graphene production techniques is given. Some potential applications of GNEMS resonators are then pointed out. The last part of the chapter is devoted to discussing the design schematics and working principles of the GNEMS resonator fabricated in this thesis. GNEMS resonators are chosen as the topic of discussion in this chapter not only because graphene was the 2D material employed to demonstrate the fabrication of 2D material based resonators in this thesis, but also because graphene is the most studied 2D material and there is fair number of published works on GNEMS resonators. However, the approaches towards GNEMS resonators should also be applicable to other 2D material based resonators depending on the targeted applications.

2.1 Graphene Production Methods

This section aims to provide a brief review of the methods used to produce graphene for GNEMS resonators. Only the well-established production approaches which have been demonstrated to produce high quality single or few layer graphene for GNEMS resonators are discussed. A more in-depth discussion about the main graphene production techniques can be found in ref. [46]. Figure 2.1 illustrates the main graphene production techniques.

2.1.1 Mechanical Exfoliation

Single layer graphene was first isolated with mechanical exfoliation where graphene is transferred to a flat substrate by pressing an adhesive tape with graphite flakes against the substrate (Figure 2.1a) [7]. It has been optimised to produce high quality graphene with sizes up to 1 mm (size of single crystal grain in graphite) [47]. Although mechanical exfoliation produces the best quality graphene and remains the method of choice for fundamental studies

and demonstrations of proof-of-concept devices, it is not suitable for large scale application as it does not produce graphene in large sheets.

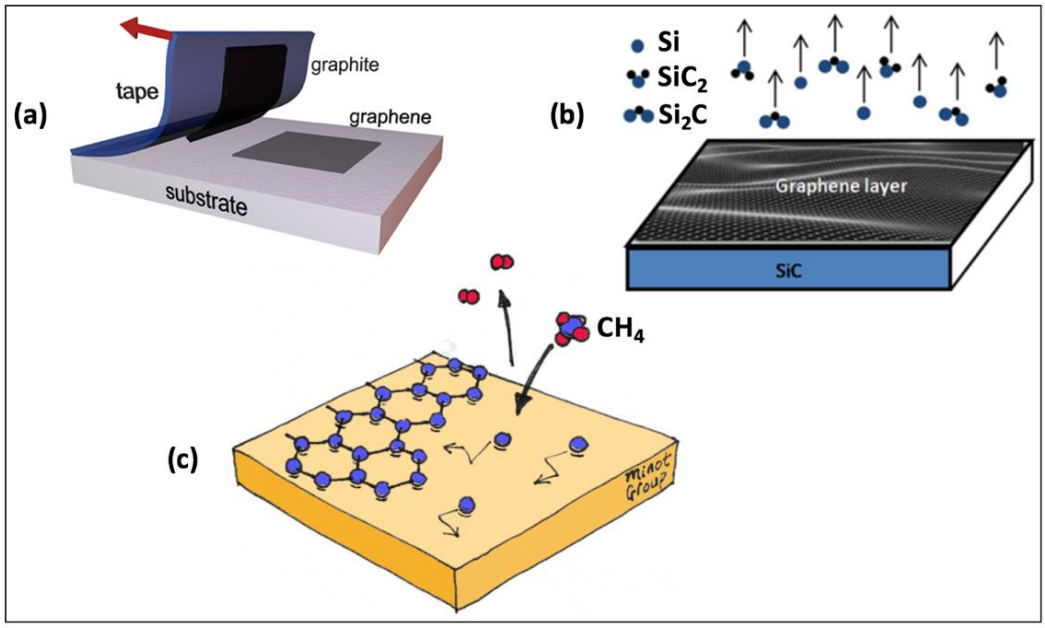

Figure 2.1: Schematics representation of graphene production methods. (a) mechanical exfoliation of graphene on a substrate by pressing a scotch tape with graphite against the substrate [91]*, (b) graphene growth on SiC substrate at high temperatures where Si evaporates and carbon atoms connect to form graphene* [92]*, graphene growth on copper by CVD with CH_4 at high temperatures* [93].

2.1.2 Epitaxial Growth on Silicon Carbide (SiC)

Graphene has been reported to be grown on SiC substrate at above 1000°C. Thermal decomposition of SiC at high temperature causes silicon (Si) to sublimate and carbon (C) atoms rearrange themselves hexagonally to form graphene (Figure 2.1b). The advantage of growing graphene on SiC is the fact that SiC is an established material for high frequency electronics [46]. However, the high cost of SiC wafers presents a challenge for large scale production of graphene. Furthermore, the growth of graphene on SiC substrates is not a self-limiting process meaning that different thicknesses of graphene may result. This makes it hard to obtain uniform single layer graphene grown on SiC.

2.1.3 Chemical Vapour Deposition

Chemical vapour deposition (CVD) is a popular method used for depositing thin films in the semiconductor industry where a substrate is exposed to a volatile precursor which decomposes to form the desired film on the substrate. CVD growth of carbon on copper (Cu) foils at more

than 1000°C with a mixture of methane (CH_4) and hydrogen (H_2) has been shown to produce large areas (300 mm Cu films) of single-layer graphene (Figure 2.1c) [47]. The process takes advantage of the fact that CH_4 can be thermally decomposed at large temperature and Cu has low carbon solubility. Also, this is a self-limiting process as the reaction stops when the all the Cu foil area is covered with graphene, leading to only 5% of the area covered with few-layer graphene [47]. One drawback of CVD graphene is that so far high-quality single- or few- layer CVD graphene can only be achieved when graphene is grown on metals. Thus, for applications involving graphene on non-metallic substrates, graphene must be transferred from the metal foil where it has been grown to the desired dielectric substrate. This extra process step could introduce defects in the graphene. An overview of the graphene transfer methods will be provided in 3.1.1.

2.2 Properties of GNEMS Resonators

As discussed in 1.1.2, graphene has all the attractive properties for NEMS resonators, including high in-plane stiffness, high breaking strain and low mass. All these superior mechanical properties mean GNEMS resonators operate at very high frequencies. For single layer GNEMS resonator with dimensions in the μm regime, the resonant frequency can be expressed as that for a membrane without bending stiffness. The following expressions are applied for GNEMS resonators which consist of suspended doubly clamped (i.e., clamped-clamped) graphene beam or fully clamped graphene membrane (i.e., drum) [39].

$$f_{doubly\ clamped} = \frac{1}{2L}\sqrt{\frac{E}{\rho}\varepsilon} \tag{1}$$

$$f_{circular} = \frac{0.766}{D}\sqrt{\frac{E}{\rho}\varepsilon} \tag{2}$$

where E, ρ, D, L, ε are graphene's Young modulus (E = 1 TPa), graphene's mass density (ρ = 7.4×10^{-9} kg/μm^2), circular graphene membrane's diameter, graphene beam's length and strain in graphene. Thus, GNEMS resonators' resonant frequencies can be increased by applying larger strain in the graphene.

Figure 2.2 shows the calculated resonant frequencies of GNEMS resonators with respect to the device's dimensions and the values of strain in graphene. Unlike NEMS resonators based on bulk materials, the resonant frequencies in the GHz range can be achieved with device dimensions in the μm range.

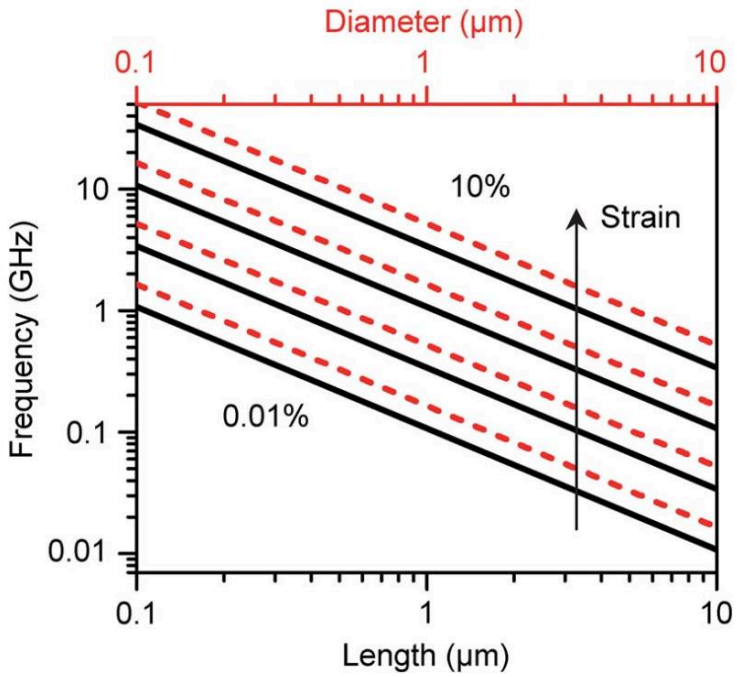

Figure 2.2: Calculated resonant frequencies for GNEMS resonators with doubly clamped graphene beam (black) or circular graphene membrane (red) for strain in graphene being 0.01%, 0.1%, 1% and 10%. Note that devices with dimensions in the μm range can achieve resonant frequencies in the GHz range for strain being around 1%.

2.3 Fabrication of GNEMS Resonators

A variety of fabrication methods to fabricate GNEMS resonators have been reported in literature. These methods vary with the way graphene is obtained and how it is suspended afterwards. The free-standing graphene within these GNEMS resonators is either fully clamped membrane or clamped-clamped beam. Note that "membrane" and "beam" both refer to mono- or few-layer graphene films. "fully clamped" refers to the fact that graphene tightly covers a cavity and is clamped on all sides while "clamped-clamped" means that graphene is suspended over a trench and clamped at both ends.

2.3.1 Fabrication of GNEM Resonators based on Exfoliated Graphene

A wide range of GNEMS resonators are fabricated based on exfoliated graphene. As pointed out in 2.1, mechanical exfoliation produces the best quality graphene and is widely used for graphene fundamental studies and proof-of-concept devices. However, it offers very little control in terms of the number of layers and sizes of the produced graphene sheets [19]. Figure 2.3 presents the SEM pictures of the fabricated GNEMS resonators based on exfoliated graphene.

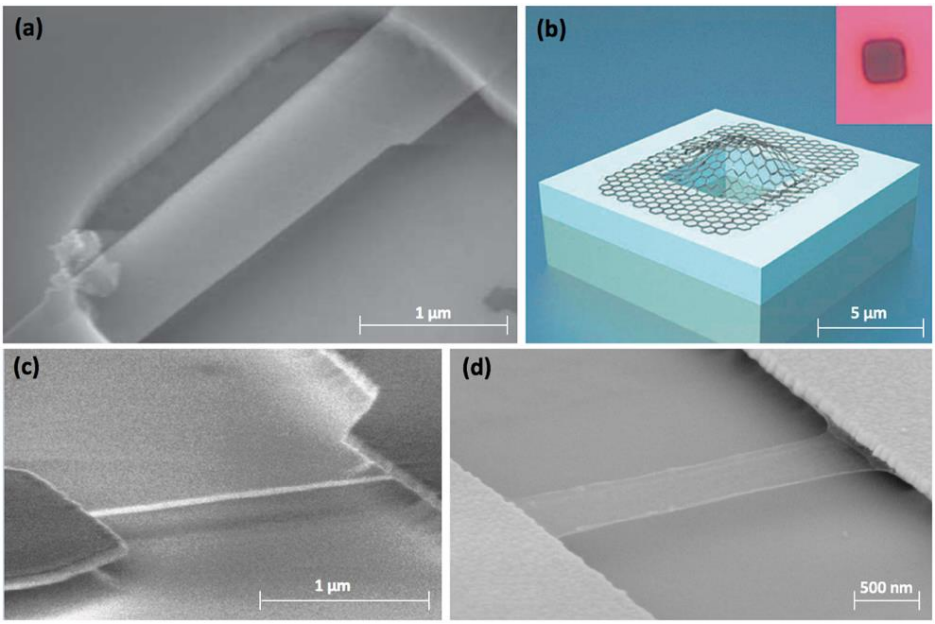

Figure 2.3: GNEMS resonators based on exfoliated graphene. (a) SEM picture: graphene exfoliated over pre-patterned trenches on SiO_2 to achieve clamped-clamped suspended beam [40], (b) cartoon: graphene exfoliated over pre-patterned square holes to achieve fully clamped membrane, inset is the optical image of the membrane [48], (c)-(d) SEM pictures: graphene is exfoliated on SiO_2, gold and graphene are lithographically patterned, graphene is suspended by etching the underlying SiO_2 [49] [50].

In the first demonstration of GNEMS resonators, the suspended clamped-clamped graphene beams were realised by exfoliating graphene onto an array of pre-patterned trenches etched into silicon oxide (SiO_2) (Figure 2.3a) [40]. Monolayer suspended graphene beams were achieved with the number of layers being verified by optical methods. By exfoliating graphene onto square wells etched into SiO_2, fully clamped suspended gas-impermeable graphene membranes were obtained (Figure 2.3b) [48]. Although this method is relatively fast in producing devices, it is not reproducible and there's no control over the shapes of the clamped-clamped suspended graphene beams.

A more controlled way of fabricating GNEMS resonators is to use lithography to pattern graphene into desired shapes (Figure 2.3c,d) [49] [50]. Graphene is exfoliated onto SiO_2 substrate and confirmed to be monolayer by optical methods before metal electrodes are patterned with lithography on top of graphene. Another lithography step is employed to define the dimensions of graphene. Clamped-clamped suspended graphene beams are achieved by wet-etching the underlying SiO_2 in buffered hydrofluoric acid (BHF) followed by a critical point drying step to avoid graphene sticking to the substrate. Despite more control over the sizes and shapes of the suspended clamped-clamped graphene beams, it is difficult to fabricate fully clamped graphene membranes with this method.

2.3.2 Fabrication of GNEMS Resonators based on Graphene derived from Large Scale Synthesis Methods

Other attempts to fabricate GNEMS resonators on larger scales involve the use of graphene derived from large scale synthesis methods. The main advantage of these methods is the fact that they can produce large-area graphene thus enabling device fabrication with mass-reproducibility. The large-area synthesis methods that have been used to produce graphene for GNEMS resonators are epitaxial growth and chemical vapour deposition.

Epitaxial graphene grown on silicon carbide (SiC)

A method for fabricating GNEMS resonators based on epitaxial graphene grown on SiC is demonstrated in Figure 2.4 [51]. Graphene is epitaxially grown on a SiC substrate at high temperature in vacuum. Gold electrodes are lithographically patterned on graphene before the graphene beam is defined with another lithography step and etching in oxygen plasma. The clamped-clamped graphene beam is released using an isotropic photoectromechanical etching procedure in a solution of aqueous potassium hydroxide (KOH) with an ultraviolet light (UV) source and the substrate as the anode (Figure 2.4e).

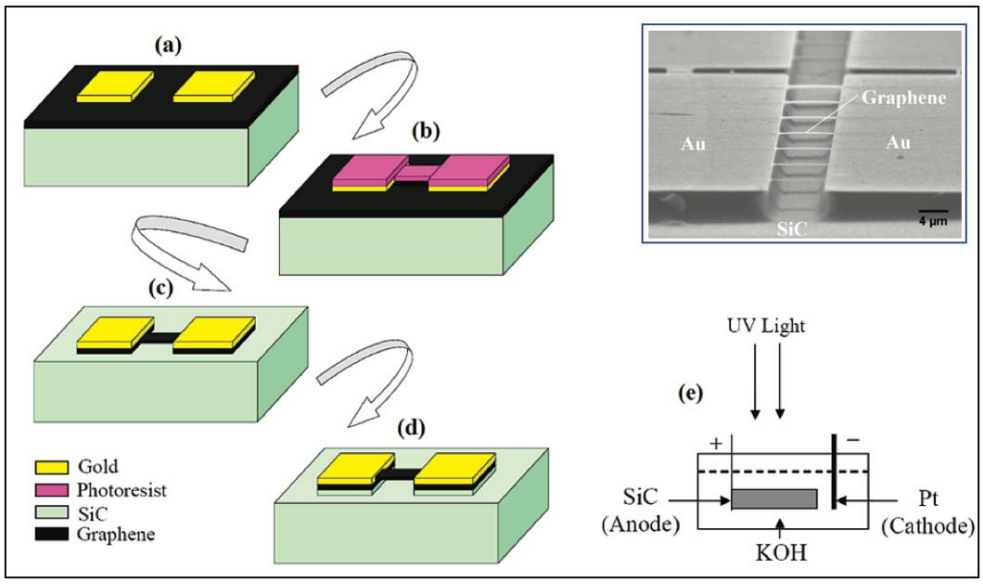

Figure 2.4: Fabrication steps for GNEMS resonators based on free-standing epitaxial graphene. (a) gold electrodes are lithographically patterned on SiC substrate with expitaxially grown graphene, (b)-(c) graphene is patterned with another lithography step and oxygen plasma etching, (d) graphene is released by etching a thickness of SiC, (e) the isotropic photoelectromechanical etching process of SiC in KOH with SiC acting as the anode. Inset on top right is the SEM picture of the fabricated array of suspended graphene [51].

As discussed in the previous section, the drawback of growing graphene on SiC is that it is hard to control the number of resulting graphene layers. In fact, the free-standing graphene in GNEMS resonators achieved in [51] is multi-layer with the thickness of 1 nm.

CVD graphene

Several studies have shown the potential of CVD as a cost-effective and scalable way to produce good-quality graphene for GNEMS resonators. Polymer supporting layers are deposited on copper foils with CVD grown graphene before the copper is etched. The supported graphene is then transferred to a desired substrate and the supporting polymer is dissolved. Ref. [44] first demonstrated the fabrication of GNEM resonators based on CVD graphene. Figure 2.5 presents the three types of obtained suspended graphene. Electrically contacted clamped-clamped suspended graphene beams are fabricated by transferring graphene on SiO_2 substrate, patterning graphene into small bars, depositing metal electrodes before releasing the graphene by wet etching of the oxide underneath graphene in BHF followed by a critical point drying step (Figure 2.5c). Fully clamped graphene membrane is achieved by transferring graphene onto suspended silicon nitride (SiN) membrane with square holes (Figure 2.5b). Graphene pre-patterned into strips on copper foiled can also be transferred on trenches etched into SiO_2 to make clamped-clamped suspended beams (Figure 2.5a) although this means less control and scalability.

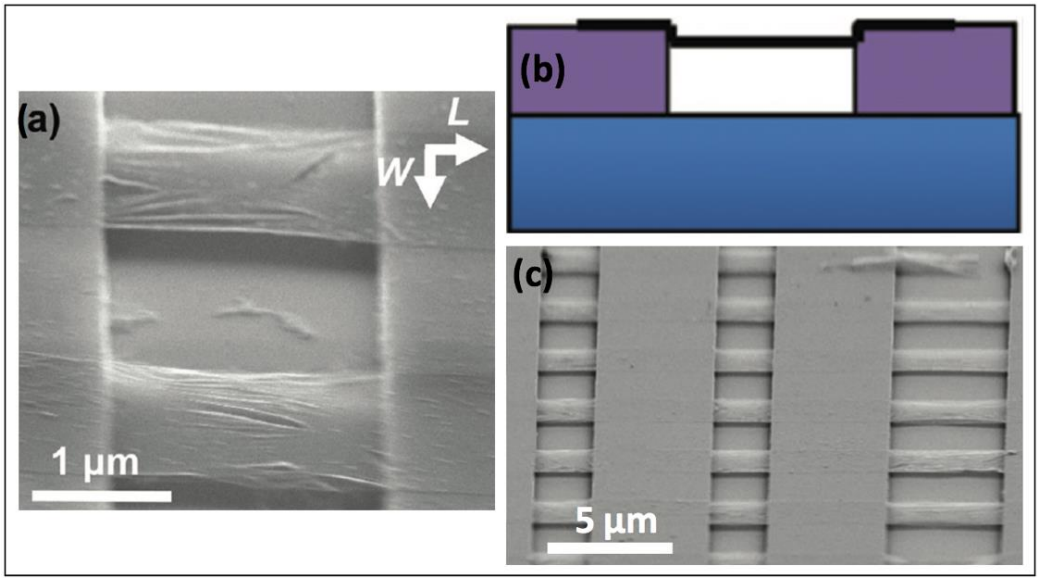

Figure 2.5: GNEMS resonators based on CVD graphene [44]. (a) SEM picture: pre-patterned graphene is transferred onto trenches etched into SiO_2 to make clamped-clamped beams, (b schematics illustration of fully clamped beam fabricated by transferring CVD graphene onto suspended SiN membrane with square holes, the side of the SiN membrane without graphene is adhered to the Si substrate, (c) SEM picture: array of clamped-clamped graphene beam is achieved by transferring graphene on SiO_2, patterning electrodes and graphene and etching SiO_2.

2.4 Actuation and Detection of GNEMS Resonators

As MEMS is scaled down to NEMS, new challenges associated with the actuation and detection of the device's resonance ensue. These challenges include the need for ultrasensitive and very high bandwidth displacement transducers and novel modes of efficient actuation at the nano-scale [3]. This section will attempt to summarise the state-of-the-art transduction mechanism employed in GNEMS resonators.

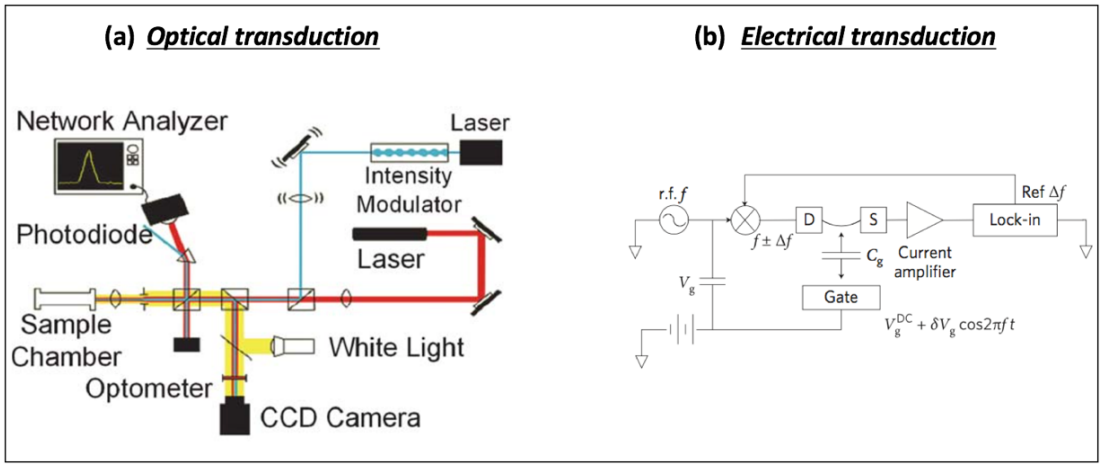

Figure 2.6: Optical transduction and Electrical transduction of GNEMS [39].

2.4.1 Optical Transduction

Figure 2.6a illustrates the optical transduction method for GNEMS resonators. The method, which was reported in [40], involves a laser driving graphene into motion. The frequency modulated laser acts to heat up the graphene, causing it to expand and contract periodically. A second laser is used to detect the motion of the graphene. This laser once directed on the graphene gets reflected off the graphene and off the substrate beneath the graphene once passing through it. This sets up an interference pattern. The interference pattern changes with the position of the moving graphene, modulating the intensity of the total reflected light. Therefore, the graphene's motion can be tracked by monitoring the intensity of the reflected signal with a fast photodiode connected to a spectrum analyser.

2.4.2 Electrical Transduction

An interesting attribute of GNEMS resonators that makes the electrical transduction possible is the dependence of the graphene's conductance on its position relative to the gate. The relation of the source-drain current with graphene's motion is expressed by the following equation [52].

$$\frac{dI_d}{dz} = V_d V_g \frac{dG}{dV_g}\frac{C_g'}{C_g} \tag{3}$$

where I_d, z, V_d, V_g, C_g, C_g' are the source-drain current, distance between graphene and gate, source-drain voltage, gate voltage, capacitance between graphene and gate, first spatial derivative of capacitance between graphene and gate, respectively. The source-drain current's dependence on the graphene's deflection is more prominent with larger gate effect on the graphene's conductance (i.e., larger $\frac{dG}{dV_g}$).

A current-mixing technique to read out the mechanical resonance was used in the first demonstration GNEMS resonators' electrical transduction where a degenerately doped Si substrate was employed as the gate electrode (Figure 2.6b) [49]. A dc voltage is applied to the gate electrode beneath the suspended graphene to cause static deflection of the graphene towards the gate, giving rise to a tension in graphene. A time-varying radio frequency (RF) voltage of frequency *f* is also applied to the gate to drive the graphene into motion with varying conductance at *f*. As the large parasitic capacitance between the Si gate and the bonding pad induces a large background RF noise signal that would impede the mechanical signal, another RF signal of frequency $f + \Delta f$ with Δf in the KHz range in applied to the drain. This results in a current with both frequency components $f + 2\Delta f$ and Δf. The Δf component is then monitored with a lock-in amplifier. The amplitude of the Δf component is given by the following equation [49]:

$$I^{\Delta f} = \frac{dG}{dV_g}\delta V_{sd}^{f+\Delta f}(\delta V_g^{f} + V_g\frac{\delta z^f}{z}) \tag{4}$$

where $V_{sd}^{f+\Delta f}$, δV_g^f, δz^f, z are the amplitude of the RF drain voltage at $f + \Delta f$, amplitude of RF gate voltage at *f*, dc gate voltage, amplitude of graphene periodic vibration at *f*, and distance between graphene and gate, respectively. A more direct electrical read-out can be implemented by eliminating the parasitic capacitance with a local back gate structure [53].

2.5 Design Schematics and Working Principles

The adopted GNEMS resonator design in this thesis consists of a suspended clamped-clamped graphene beam, as illustrated in Figure 2.7. Unlike most of the studies on GNEMS resonators, where graphene is clamped between the source/drain electrodes and the underlying oxide, here the suspended graphene lies on top of the electrodes. The good clamping is obtained by the van der Waals interaction between graphene and gold. This interaction also causes the

graphene to stick to the gold's wall. A degenerately doped wafer is employed as the conductive back-gate. A back-gate metal electrode can be implemented to tackle the parasitic capacitance which impedes a direct electrical transduction of the resonator [53] [54]. A silicon oxide layer between the source/drain and gate electrodes provide electrical insulation.

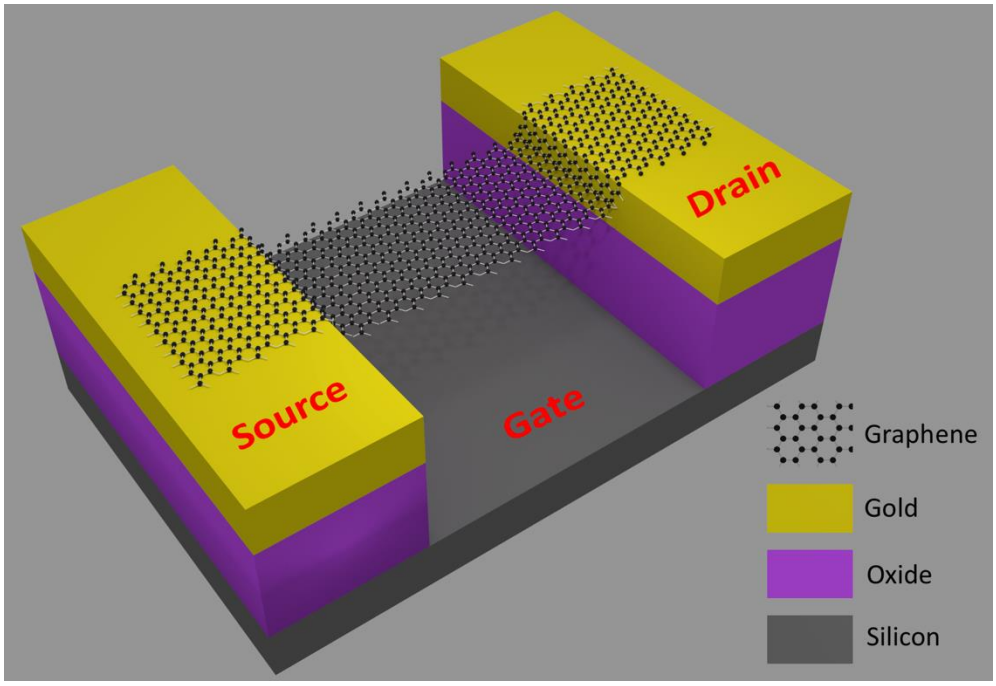

Figure 2.7: Schematics of the designed GNEMS resonator. Free-standing graphene is achieved by placing graphene on top of source/drain electrodes and suspending it over back-gate highly doped silicon substrate. Oxide layer provides electrical insulation.

In contrast to the approach mentioned in ref. [44], where CVD graphene is pre-patterned on copper foil into strips before these graphene strips are transferred to trenches etched into SiO_2 to obtain clamp-clamped beams, the design presented in Figure 2.7 facilitates the much more scalable and reproducible fabrication of CVD graphene based GNEMS resonators. A major number of the fabrication steps to pattern electrodes are done on the wafer scale. CVD graphene is later transferred and patterned onto substrates with these electrodes before being released to make free-standing graphene beam. As the transfer of CVD-grown graphene from copper foils to the desired substrate has been demonstrated to be possible for up to 300 mm diameter wafer [55] [56], there is a potential for all fabrication steps to be carried out on the wafer level. This can greatly reduce the cost and time involved in fabricating graphene based devices on large scales. Furthermore, the fact that graphene is only involved in the last steps of the fabrication process implies the minimal exposure of graphene to fabrication-related materials which are known to introduce defects to graphene and degrade its properties. The details of the device fabrication procedure will be discussed in the next chapter.

As pointed out in the 2.4, together with the optical methods, the metal electrodes implemented in our device facilitates the electrical transduction of the device's resonant motion. Also, these electrodes make it possible to investigate the quality of the fabricated graphene by measuring its electrical properties such as graphene's sheet resistance as well as the gate effect where where electrostatic gating influences graphene's conductance. These electrical measurements are presented in 4.1.

In summary, a design of 2D material based NEMS resonators was proposed. Graphene was chosen to demonstrate the design and fabrication of GNEMS, which consist of a free-standing doubly clamped graphene beam. A fair amount of research being conducted on GNEMS resonators has demonstrated the possibility of the efficient optical and electrical actuation and detection of the GNEMS's resonance. The clamping of graphene on top of metal electrodes is predicted to significantly reduce the number of fabrication steps and minimise the exposure of graphene to the sacrificial layers during fabrication.

Chapter 3

Graphene Transfer and Device Fabrication

The goal of this chapter is to provide a detailed description on how the device envisioned in 2.5 is fabricated. In the first part of this chapter, a short overview of graphene transfer methods is followed by a discussion about the adopted graphene transferring procedure. The second part of this chapter begins by introducing the common graphene patterning techniques and graphene characterisation with Raman spectroscopy. Also, details on the employed graphene patterning method and how it is optimised are presented. Subsequently, a discussion about the process flow and fabrication steps is given. The chapter concludes with a review of the encountered issues during device fabrication and the solutions for them. Detailed fabrication run sheets and recipes are presented in Appendix A while the distribution of devices on wafers and chips can be found in Appendix B.

3.1 Graphene Transfer

3.1.1 Overview of Graphene Transfer Methods

As discussed in 2.1, among the large-scale synthesis methods of graphene, CVD has been demonstrated to produce dominantly single-layer, large-grained graphene and available at low costs. CVD graphene on copper foils was therefore used in this project for device fabrication. To start making devices from graphene, graphene from the growth substrate should be transferred to a target substrate for further processing. Ideally, CVD graphene should be grown directly on the target substrate. This, however has not been realised yet for non-metallic substrates [46]. Various methods exist for the transfer of CVD graphene. These methods can be categorised into “wet” or “dry” methods, depending on the medium in which graphene is transferred onto a target substrate [57]. Transferring graphene on a desired substrate relies heavily on polymers as supporting layers. Poly(methyl methacrylate) (PMMA) appears to be the most common supporting polymer for graphene transfer owing to its low viscosity, strong wetting capability, good flexibility, and good dissolubility in a number of organic solvents [58]. Since CVD graphene is often grown on both sides of a metal foil, the transfer process starts with coating PMMA on one side of the metal foil and etching the graphene on the other side.

In wet transfer, the metal is etched in an acid solution before the PMMA/graphene film is transferred from the aqueous solution to a target substrate. PMMA is dissolved away by an organic solvent at the end of the process to reveal graphene sitting on a substrate. Dry transfer is often enabled by polydimethylsiloxane (PDMS) stamp where the stamp serves as a handle to manipulate the metal/graphene/PMMA film and later is peeled off once the metal has been etched and the graphene/PMMA film has been transferred onto a target substrate [59] [60]. PMMA is then thermally removed in a furnace at high temperature. Dry transfer is preferred when graphene is transferred onto closed wells due to the potential of trapping liquid inside the wells if wet transfer is used [60]. Figure 3.1 summarises the main differences between the wet and dry transfers. The wet transfer method with PMMA being the support material is employed in this thesis since the substrates on which graphene is transferred to do not have closed wells. Details of this transfer method will be discussed in the next section.

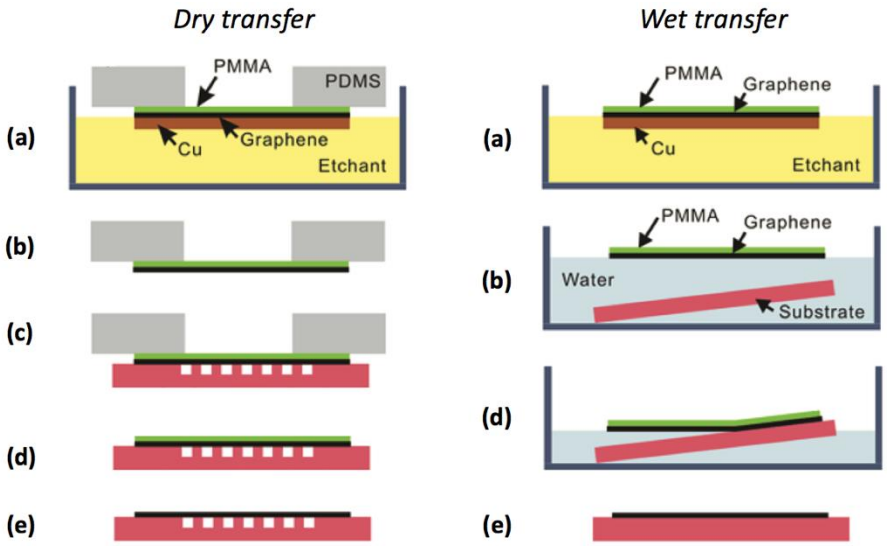

Figure 3.1: Dry transfer vs. wet transfer, adapted from [60]. Dry transfer: (a)-(b) protective PMMA is coated on one side of the copper foil having graphene on both sides and graphene on the other side is etched, a PDMS block is then attached to the PMMA/graphene/copper film by natural adhesion and the copper is etched in an etchant solution (c) PDMS is used as a handle to place the PMMA/graphene composite onto a substrate, (d) PDMS is peeled off and PMMA is heat treated to enhance contact with the substrate (e) graphene is thermally removed in a furnace. Wet transfer: (a) protective PMMA is coated on one side of the graphene/copper/graphene film and the graphene on the other side is etched, the PMMA/graphene/copper film is left in an etchant solution to dissolve away the copper, (b)-(c) the PMMA/graphene composite is wet-transferred onto a substrate, (d) PMMA is removed in an organic solvent.

3.1.2 Employed Graphene Transfer Procedures

Since there are no cavities or wells that need to be encapsulated by graphene on the substrate, a wet transfer procedure is used. Figure 3.2 summarises the transfer procedure to

place graphene onto a target substrate in this project. As will be discussed in the fabrication section 3.2, the target substrates are oxide chips for transfer optimisation and oxide chips with electrodes for device fabrication. 3 cm × 5 cm copper foils with mono-layer graphene grown by CVD on both sides are provided by the crystal growth facility at the EPFL's institute of physics (IPHYS).

PMMA is spin-coated on one side of the graphene/copper/graphene film to later provide mechanical support for the graphene. Firstly, the film is placed and pressed to straighten out on a wafer with coated PDMS. Due to its sticky behaviour, PDMS acts to form good contact with the film which, once pressed against the PDMS surface with a cloth, lies flat on the wafer. A solution of 4% PMMA in anisole solvent is then dispensed carefully all over the film. Spin coating is performed at the speed of 3000 revolutions per minute (rpm) for 2 minutes with the acceleration of 1066 rpm per second. The wafer is soft-baked on a hot plate at 80°C for 20 minutes. The resulting thickness of the spin-coated PMMA is around 300 nm. It was found that smaller PMMA thicknesses yield better transferred graphene. The reason for this will be discussed below. After the PMMA is cured, the graphene on the side of the PMMA/graphene/copper/graphene film not covered by PMMA is etched away in oxygen (O_2) plasma (Diener Electric Zepto LF) at 50 watts for 2 minutes. The PMMA/graphene/copper film is cut into several square-shaped pieces of around 10 × 10 mm in dimension. This is because graphene will be eventually transferred onto 10 × 10 mm substrates.

The 10 × 10 mm PMMA/graphene/copper film are let floating with the PMMA side facing up in a solution of ammonium persulfate ($(NH_4)_2S_2O_8$), pH = 4 to etch away the copper. For efficient copper etching, the PMMA/graphene/copper film should lie flat to maintain good contact with $(NH_4)_2S_2O_8$. After the all the copper has been etched, the PMMA/graphene film is transferred to a beaker of deionised (DI) water for rinsing. It is important that the film be rinsed with water several times to get rid of the copper ions which could contaminate the graphene. The PMMA/graphene film is transferred to two other beakers of DI water before being fished onto the target substrate. All the above-mentioned transfers of films are facilitated by a glass slide.

The target substrate is carefully cleaned in acetone, IPA, and water before being treated in O_2 plasma (Diener Electric Zepto LF) at 100 watts for 5 minutes. The plasma treatment serves to eliminate the organic residues and render the substrate hydrophilic, which provides better adhesion of the graphene to the substrate. The PMMA/graphene film is then fished onto the target substrate from a beaker of DI water. The composite PMMA/graphene/substrate is

baked above PMMA's glass transition temperature at 150°C for 14 hours. After being transferred on the target substrate, the PMMA/graphene film does not lie flat on the substrate. The insufficient contact between this film and the substrate causes cracks and tears in the graphene when the polymer is removed. Heating the film above the PMMA's glass transition temperature renders the film flexible and flattened out thus preventing the formation of cracks and tears upon removal of PMMA [7]. As mentioned earlier, the smaller thicknesses of PMMA are favourable. This is because the thinner the PMMA the easier for the PMMA/graphene film to become flat and form good contact with the substrate after the baking. PMMA is subsequently removed in acetone overnight. The substrate with graphene is rinsed in IsoPropyl Alcohol (IPA) and water and left to dry.

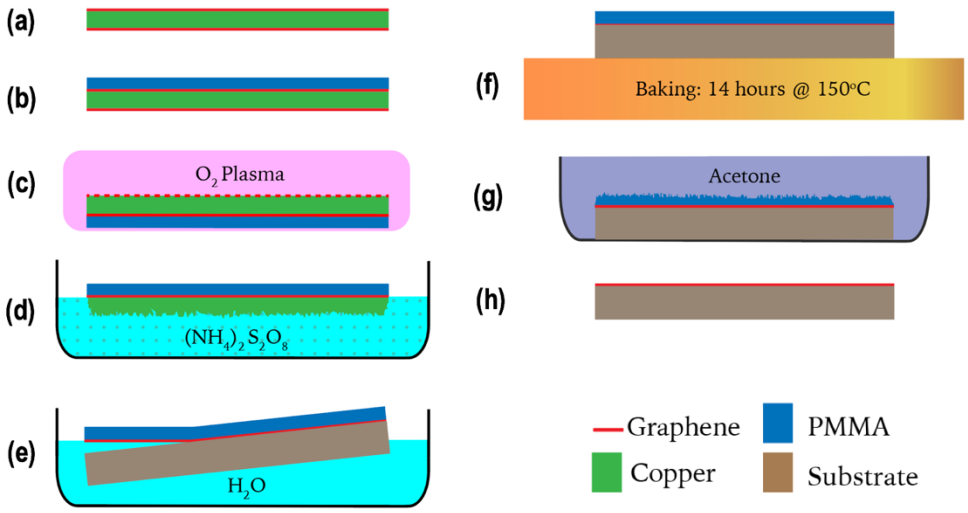

Figure 3.2: Details of the adopted graphene transfer procedure. (a) CVD graphene available on both sides of a copper foil, (b) PMMA is spin-coated on one side of the graphene/copper/graphene film, (c) the graphene uncovered by PMMA is etched away in O_2 plasma, (d) copper is etched in a solution of $(NH_4)_2S_2O_8$, (e) the PMMA/graphene film is fished onto a target substrate, (f) the PMMA/graphene/substrate composite is baked at 150℃ for 14 hours, (g) PMMA is removed in acetone, (h) graphene has been transferred on the target substrate.

3.2 Device Fabrication

3.2.1 Overview of Graphene Patterning and Graphene Characterisation with Raman Spectroscopy

The production of graphene-based devices requires that graphene be patterned into flexible shapes with flexibility and control of location and orientation [61]. Available methods of patterning graphene include "lithography", "transfer-printing" and "direct write" [62]. The

direct write method utilises a focused beam laser to produce patterned graphene oxide (GO) by heating and dissolving the exposed region into volatile gases. The patterned GO can be subsequently reduced to graphene with hydrazine gas or annealing [63]. Although this graphene patterning technique ensures the minimal exposure to resist and thus limits surface contamination in the patterned graphene, the direct writing can only be executed on graphene oxide [64]. Similarly, transfer-printing is restricted to graphene oxide as the graphene source, transfer layer and target substrate [65].

Lithography is a well-established for patterning in microelectronics and have been demonstrated to produce patterned graphene structures with high precision and scalability and with dimensions as small as 20 nm [61] [66]. One important drawback of patterning graphene with lithography is the exposure of graphene to photoresist, which influences the intrinsic properties of the patterned graphene due to polymeric residues. Nevertheless, because of its availability and readiness, standard photolithography is used to pattern graphene in this thesis. The cost and lead time of lithography mask fabrication can be compensated by employing mask-less photolithography where the radiation used to expose the photoresist is not transmitted through a mask but is provided by a narrow laser beam [67]. Although owing to cost and time reasons, standard photolithography is employed to pattern graphene in this thesis, electron beam (e-beam) lithography can be utilised in the future to produce smaller device dimensions.

Raman spectroscopy has been proven to be a useful tool for characterising the quality of graphene in terms of the number of layers and the presence of defects. It is non-destructive and provides instructive information regarding the structural and electronic properties of graphene with high resolution [68]. Figure 3.3 shows the typical Raman spectra of graphite and graphene with 532 nm excitation. In graphene, the G band is characteristic of the in-plane vibrational mode of the sp^2 hybridised carbon atoms constituting the graphene sheet, whereas the 2D band represents a two-phonon lattice vibrational process. The D band represents a ring breathing mode from the sp^2 carbon rings in the graphene lattice. Thus, D band's intensity is proportional the level of defects in the samples. The peak intensity ratio between the G and 2D band I_{2D}/I_G can be used to identify single layer graphene, namely, I_{2D}/I_G equals 2 for high-quality defect-free single layer graphene [69].

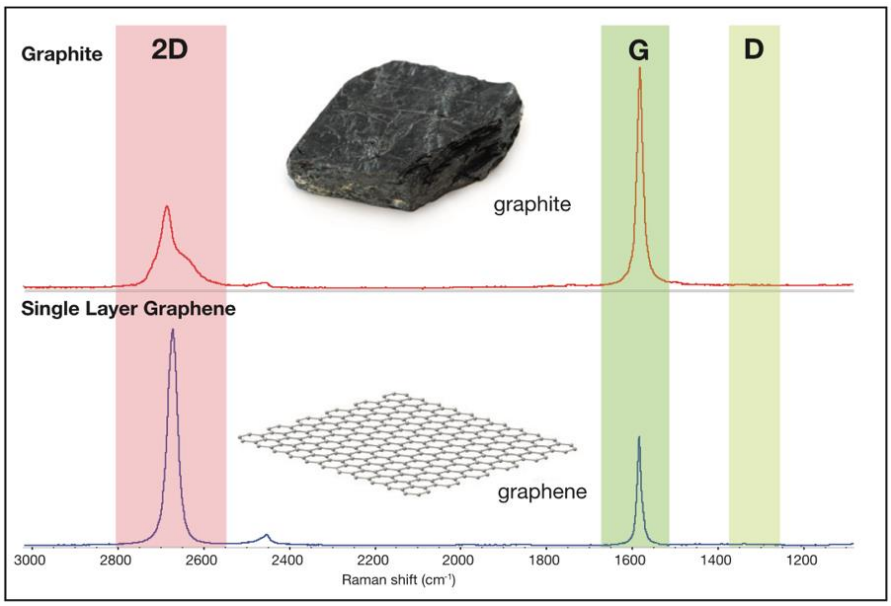

Figure 3.3: Raman spectra of graphite and graphene [69].

3.2.2 Graphene Patterning Optimisation

With the transfer procedure described in 3.1.2, graphene was transferred onto a test 10 × 10 mm silicon (Si) substrate with 290 nm wet thermal oxide (SiO_2). This thickness of oxide was chosen to ease the visual detection of the graphene under the optical microscope [70]. Coordinates are patterned into the oxide by photolithography and wet etching in buffered hydrofluoric acid (BHF) 7:1. These patterned coordinates are useful to locate specific positions on the chip in microscopes. The fabrication steps to make the test oxide substrates are detailed in Appendix A.

Photoresist of 1 µm thickness is lithographically patterned on the substrate with graphene and serves as a mask. Graphene not covered by the photoresist is etched away in O_2 plasma and the resist is stripped in a standard resist removal solution. More details on this fabrication step are discussed in Appendix A. Graphene is patterned into continuous lines, squares and circles of different dimensions. Figure 3.4 shows a scanning electron microscope (SEM) picture of the graphene patterned in O_2 plasma at 100W for 2 minutes. The squares' side lengths range from 2 µm to 640 µm. The circles' diameters range from 2 µm to 600 µm. The lines' widths range from 2 µm to 200 µm.

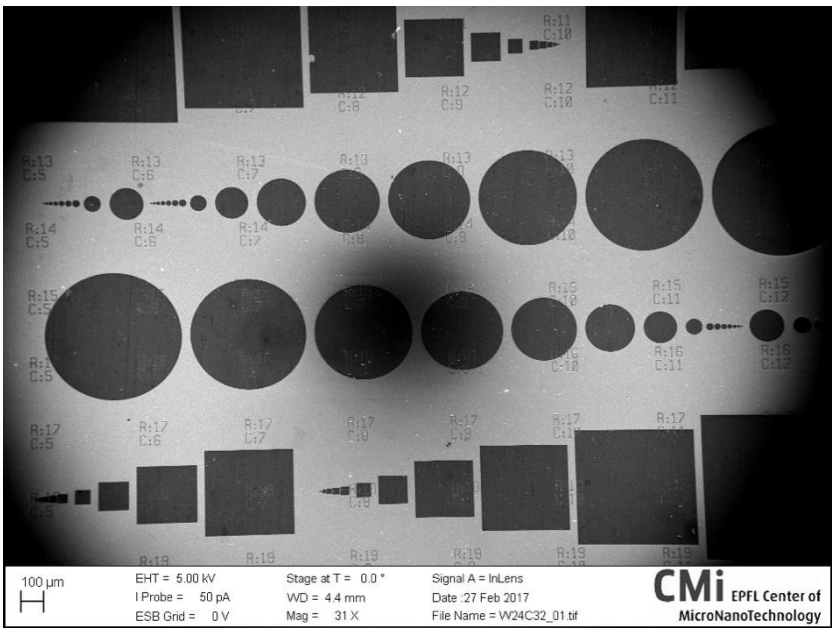

Figure 3.4: Patterned graphene of different shapes and sizes on SiO2. The squares' side lengths range from 2 µm to 640 µm. The circles' diameters range from 2 µm to 600 µm. The lines' widths range from 2 µm to 200 µm.

The higher O_2 plasma power and etching time lead to the more efficient removal of the exposed graphene but introduce the risk of unnecessarily heating up the substrate. Heating up the substrate could cause the masking resist to crosslink and render it harder to be removed. With a fixed value of O_2 plasma power at 200 W, a test was done on how the etching time affects the removal efficiency of the exposed graphene and the quality of the unexposed graphene after the resist is stripped.

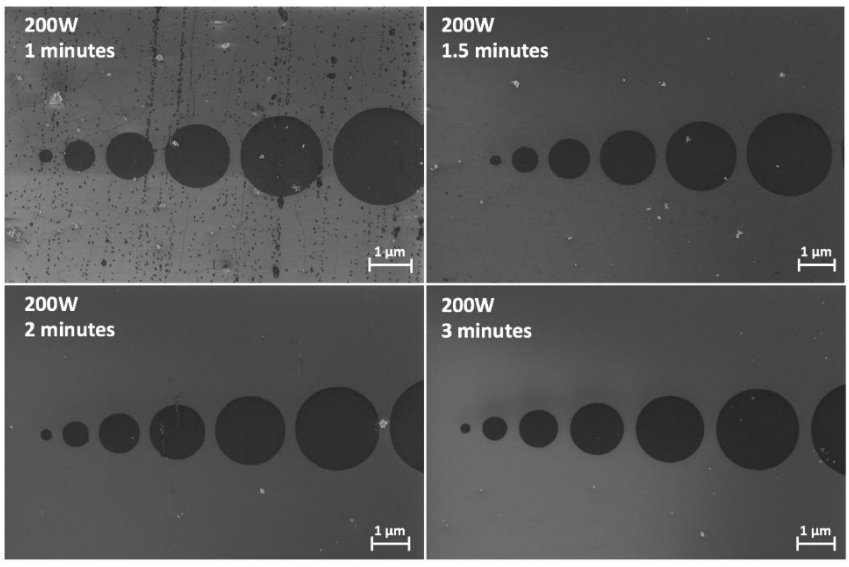

Figure 3.5: Graphene patterning results in O_2 plasma on different chips at 200 W for 1, 1.5, 2 and 3 minutes. Graphene exposed to O_2 plasma is not completely etched for etching time being 1 and 1.5 minutes.

Figure 3.5 presents the results of patterning graphene in O_2 plasma on different chips at 200 W for 1, 1.5, 2 and 3 minutes. As predicted, longer etching times result in cleaner areas

outside of the patterned graphene circles. A lot of graphene is left un-etched for etching time being 1 minute whereas a visible pattern of graphene grain boundaries is observed for etching time being 1.5 minutes.

While all the graphene exposed to O_2 plasma should be removed after this etching step, it is important to protect the resist from being overheated and crosslinked. Raman spectroscopy was performed to characterise the patterned graphene's quality. Figure 3.6 presents the intensity peak ratio map of a rectangular area on the substrate and the Raman spectra for 3 arbitrary points. The rectangular window spans both the patterned graphene and the area where graphene is expected to be completely removed. The Raman spectra of the points (X = 2, Y = 6) and (X = 6, Y = 6) are characteristic of graphene whereas the Raman spectrum for the point (X = 5, Y = 2) indicates this point is depleted of graphene. The spectra of all the points in the measurement window were investigated and it was confirmed that the graphene has been correctly patterned.

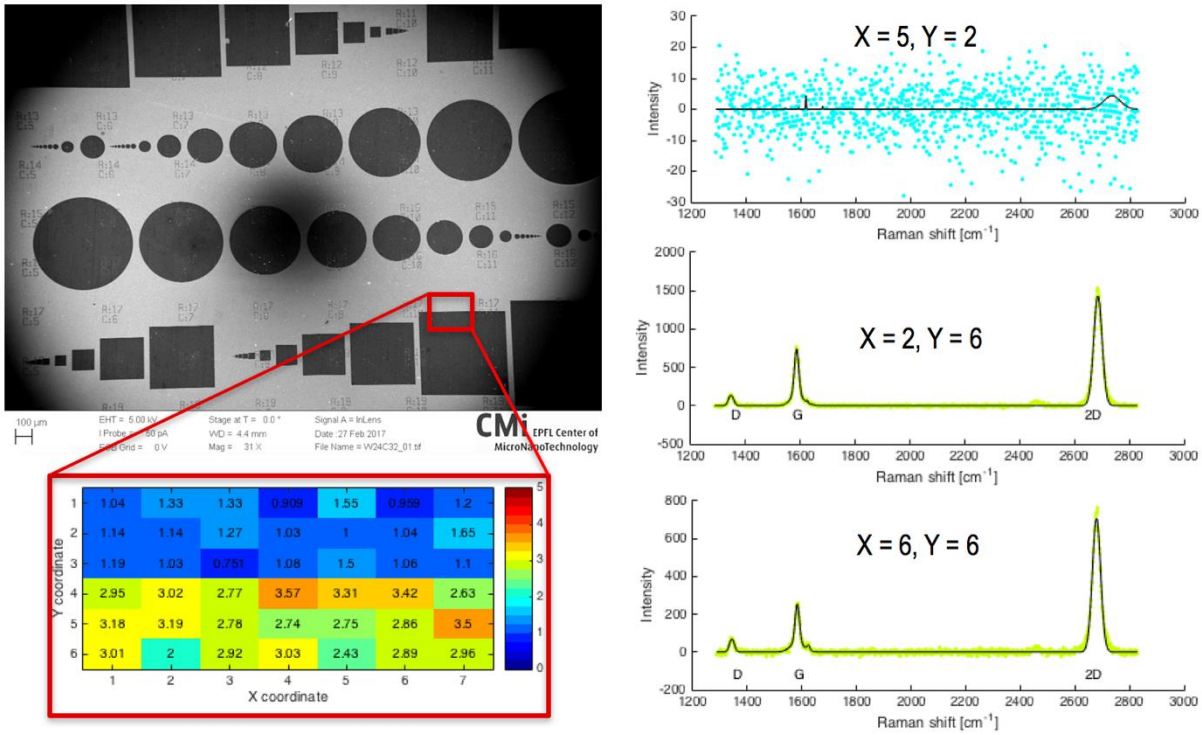

Figure 3.6: Peak intensity ratio map of a rectangular area on the substrate and the Raman spectra of three arbitrary points within this area. The rectangular window encompasses both the graphene and the area where graphene should be completely etched. Note that these spectra are representative of the points in the upper half and lower half of the measurement window. Raman spectroscopy was performed with the excitation laser of 532 nm.

As discussed before, for high-quality defect-free single layer graphene the peak intensity ratio I_{2D}/I_G should be 2. This is not the case for the above Raman spectroscopy

characterisation of the patterned graphene, where the peak intensity ratio varies between 2 and 3.5. Also, as indicated in Figure 3.6, D bands with appreciable peak intensities were observed in the Raman spectra. Besides the resist residues and defects that are introduced during graphene transfer and photolithographic patterning, the deviation from perfect graphene can be attributed to CVD graphene being used. CVD graphene have been shown to be prone to defects such as cracks, wrinkles, boundary grains and multilayer patches [71]. Figure 3.7 shows the variation in the intensity ratio I_{2D}/I_G with respect to the etching time being 1, 1.5, 2 and 3 minutes. There is a clear trend in the deviation from 2 of I_{2D}/I_G with increasing etching time. The patterned graphene used to make devices in this thesis was patterned in O_2 plasma at 200 W for 2 minutes.

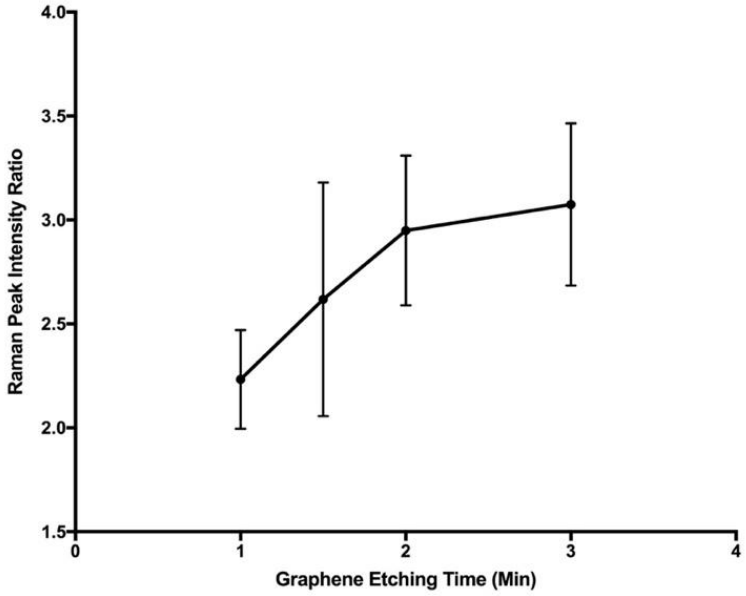

Figure 3.7: Raman peak intensity ratio of 2D band to G band for etching time being 1, 1.5, 2 and 3 minutes. The higher etching times correspond to the intensity peak ratio being further from 2, indicating a decline in graphene quality.

3.2.3 Process Flow

This section aims to give a detailed discussion about the process flow and the implemented fabrication steps. The encountered fabrication issues and the solutions for them are presented in 3.2.5. A thorough description of the fabrication steps and the optimised recipes are given in the fabrication run sheet in Appendix A. The devices were fabricated at the EPFL's Center of Micronanotechnology (CMi) clean room facility.

Figure 3.8 illustrates the fabrication process flow implemented for the fabrication of the GNEMS resonator discussed in 2.5. The process flow involves 2 lithography steps to pattern the metal electrodes on the wafer level (Figure 3.8b) and to pattern the graphene on the

chip level (Figure 3.8d). The starting point is a ∅100-mm single side polished (SSP) test p-type (0.1 - 100 Ohm.cm) Si wafer with 290 nm thick wet thermal oxide on both sides. The degenerately doped wafer is used to facilitate the subsequent implementation of the Si substrate as the gate electrode.

In the first lithography step, 1.1 μm thick positive photoresist and 0.48 μm thick lift-off resist (LOR) are spin-coated and patterned on top of the wafer with SiO_2. It is crucial that the patterned positive photoresist/LOR be slightly overdeveloped. This is to avoid the formation of fences at the edges of the source and drain patterns after lift-off as these fences could break the graphene at the edges later when the graphene is transferred and released [54]. Next, a layer of 10 nm thick chromium (Cr) and 100 nm thick gold (Au) is evaporated on the patterned photoresist. Having a layer of Cr between Au and the substrate enhances the adhesion of the gold to the substrate. The advantage of using gold as the material for the electrodes is that gold has good conductivity and does not oxidise in air. Also, gold is not corroded in O_2 plasma as opposed to other metals such as copper (Cu) and silver (Ag). An alternative for gold as the material for electrodes is platinum (Pt) which is more expensive and thus not used in this thesis. Lift-off is done to produce patterns of source and drain electrodes. A system of x- and y- coordinates, dicing marks and lithography alignment marks for chips and wafer are also patterned in Au during this step. An illustration of the device coordinates and dicing and alignment marks are provided in 3.2.4 where the mask design is discussed. The oxide on the back side of the wafer is then stripped in BHF and the wafer is diced into 10×10 mm chips.

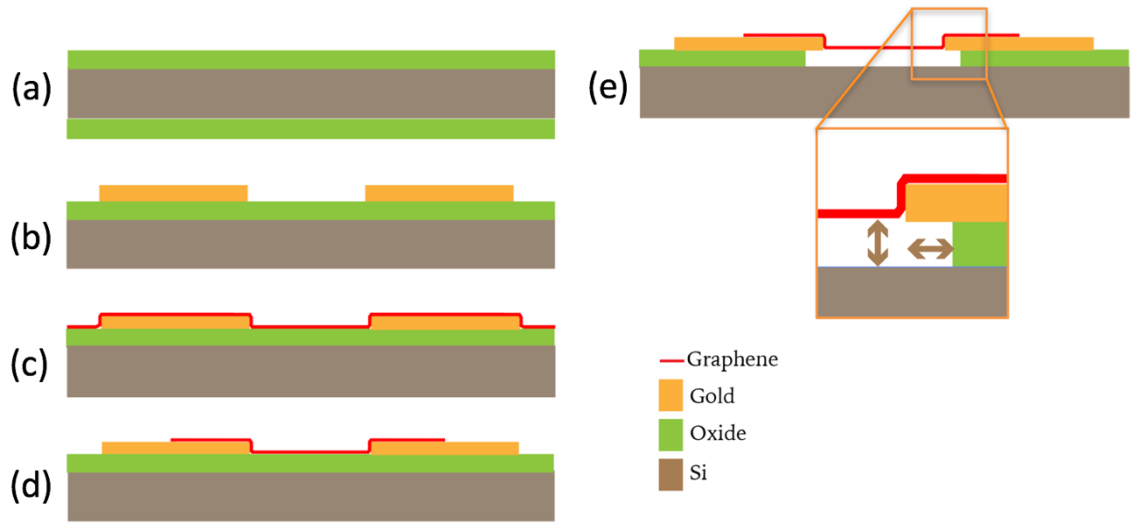

Figure 3.8: The fabrication process flow. Wafer level: (a) the starting point is a highly doped silicon wafer with 290 nm thick thermal wet oxide on both sides, (b) source and drain electrodes are patterned with lithography and lift-off, the oxide on the back side is removed in BHF, the wafer is diced into 10×10 mm substrates. Chip level: (c) graphene is transferred onto the substrate with patterned electrodes, (d) graphene is lithographically patterned to make unsuspended graphene beam across the source and drain electrodes, (e) graphene beam is suspended by etching all the oxide underneath the graphene in BHF and critical point drying the sample. Note that the oxide etching below the graphene is uniform and the same distance is etched into the oxide area underneath the source and drain electrodes. The degenerately doped substrate acts as the gate electrode.

With the graphene transfer procedure described in 3.1.2, graphene is transferred onto the chips with patterned source and drain electrodes. In the second lithography step, the transferred graphene is then patterned into unsuspended beam lying on SiO_2 and across the source and drain electrodes (Figure 3.8d) using the lithographic patterning method delineated in 3.2.1. It was found that small contact areas between the Au electrodes cause patterned graphene to be delaminated once the resist is stripped. This delamination issue will be discussed in 3.2.4. Therefore, a graphene-Au contact area equal ≈ 40% the total Au contact is applied. Higher graphene-Au contact area also helps enhance the graphene-Au contact resistance.

Having unsuspended graphene lying across the source and drain electrodes, the next step is to release the graphene to make devices. Two methods of releasing graphene to make suspended graphene beam were investigated in this thesis, namely, vapour hydrofluoric (HF) etching of SiO_2 and BHF wet etching of SiO_2 followed by critical point drying (CPD). The latter produced better results and was the method of choice in this thesis. As seen in Figure 3.8 the uniformity etching of oxide underneath the graphene can be achieved. This is because HF diffuses fast across the graphene – SiO_2 interface and starts etching SiO_2 downward at the

normal rate [72]. The issues related to releasing graphene with vapour HF etching and the optimisation of wet etching and CPD will be discussed in 3.2.5.

3.2.4 Mask Design

The lithography masks used in this project were designed in the layout tool Tanner L-Edit. Since two photolithography steps to pattern the source/drain electrodes and graphene are required, the employed mask consists of two layers. Figure 3.9 presents a typical device constituted of two layered patterns for source/drain electrodes and graphene. Several devices of different lengths and widths are swept across the chip. The total number of viable devices on a single 10×10 mm chip is 640. The details on these varied dimensions are given in 3.2.6. The distribution of devices on a chip and chips on a wafer are described in Appendix.

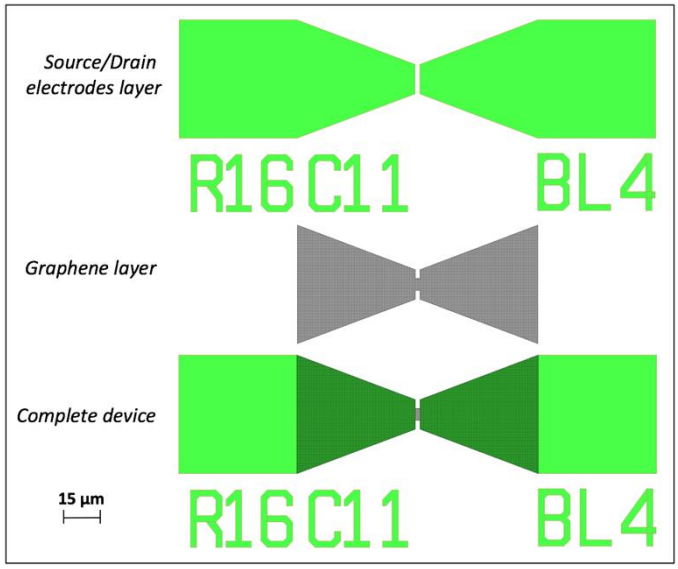

Figure 3.9: L-Edit layout representation of the layers used in the fabrication mask. "R16C11" represents the lateral coordinates of this device on the chip which is at row 16 and column 11. "BL4" indicates the designed beam length (i.e., the length of the graphene beam) is 4 µm.

Other mask structures that are essential during the device fabrication include chip and wafer lithography alignment marks, wafer dicing alignment marks, and exposure grids for photolithography exposure test. These structures illustrated in Figure 3.10. The exposure tool used in this project (Heidelberg Instruments Maskless Aligner MLA150) possesses the image processing capability to detect the centres of the alignment marks which have been patterned on the chip. Although standard photolithography is used, a set of e-beam lithography alignment marks were included on the chip in case e-beam lithography must be employed.

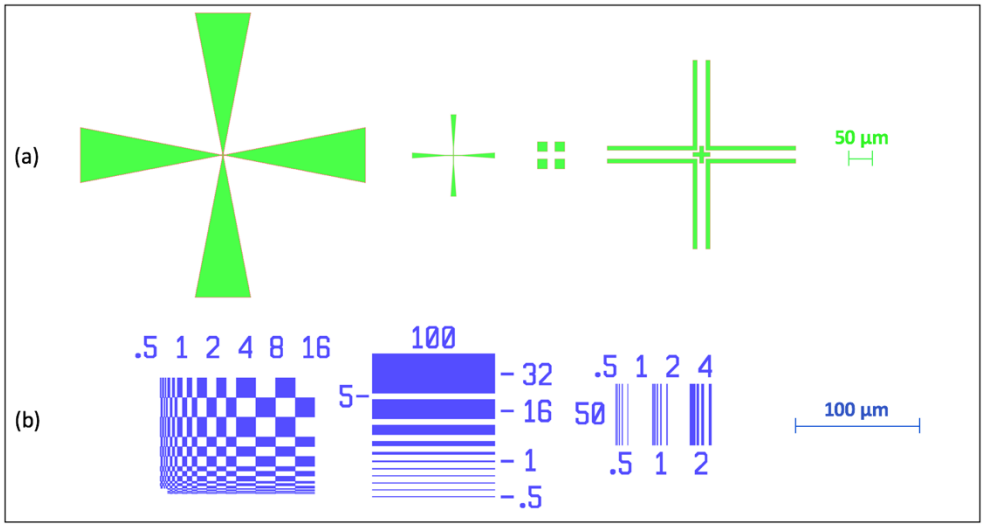

Figure 3.10: Miscellaneous mask structures. (a) from left to right: lithography alignment marks for wafer and chip, chip e-beam lithography alignment mark and wafer dicing mark, (b) exposure grids for photolithography exposure test and photolithography result verification.

3.2.5 Encountered Issues and Solutions

3.2.5.1 Delamination of Graphene during Resist Stripping

As discussed in the previous section, the contact area between graphene and Au affects the adhesion of the graphene to gold. Figure 3.11a shows the graphene patterning results on the substrates with Au pads for small and large graphene-Au contact areas. In Figure 3.11a, the red rectangle represents the resist/graphene pattern before the resist was stripped. The graphene was lifted together with the resist and only the part of the graphene beam in contact with the oxide remained. The graphene indicated by the black oval was covered by photoresist which was not developed and thus was not etched by O_2 plasma. This indicates that graphene was not susceptible to the resist removal solution and the graphene delamination was not due to graphene reacting with the removal solution.

Figure 3.11b shows the SEM picture of a patterned graphene after resist stripping for a larger graphene-Au contact area. It can be noticed that both the graphene parts in contact with the gold and the oxide were successfully patterned.

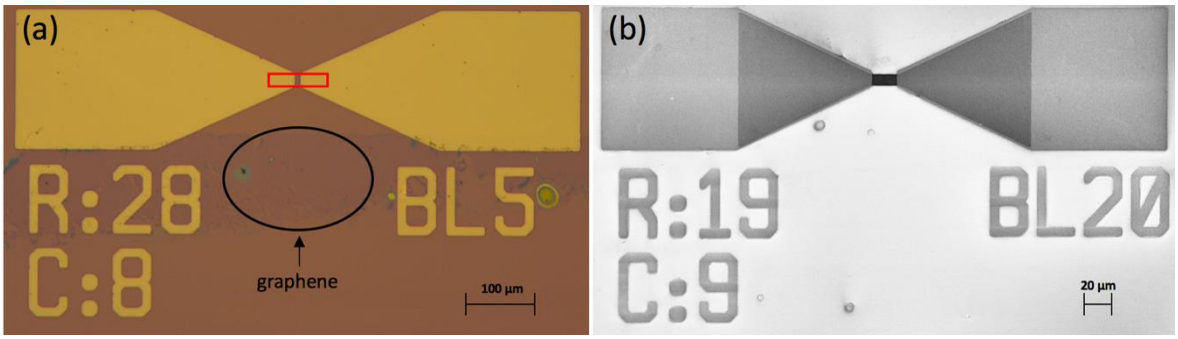

Figure 3.11: Graphene patterning results for small and large graphene-Au contact areas. (a) Small graphene-Au contact area: delamination of graphene from the Au pads when resist was stripped. The red rectangle represents the original graphene pattern. The remaining graphene indicated by the black oval was covered by undeveloped resist and thus remained after the resist was stripped. (b) Large graphene-Au contact area: both the graphene parts in contact with the Au pads and oxide were successfully patterned.

3.2.5.2 Resist Residues

It is important that the resist is appropriately stripped since remaining polymer residues could have deteriorating effect on graphene performance. Results of resist stripping by different resist removal solutions are compared in Figure 3.12. The removal solutions used were acetone, Microposit Remover 1165 and TechniStrip P1316. Stains of resist on several devices can be observed for the chip with resist stripped by acetone. This is because the high vapour pressure of acetone induces fast-drying and re-deposition of removed resist on the substrate as striation [73].

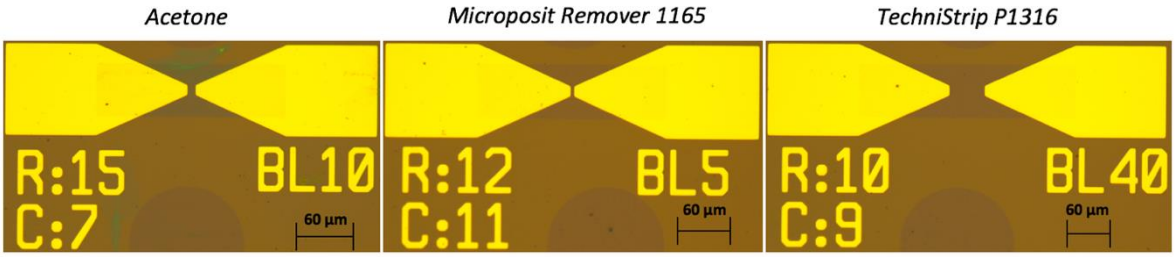

Figure 3.12: Comparison of graphene patterning results when resist is stripped by different resist removal solutions. Microposit Remover 1165 and TechniStrip P1316 have better resist removal performance whereas acetone leaves behind some re-deposited resist. The circular patterns outside the devices were meant to test the adhesion of graphene to oxide. Images were taken with an optical microscope.

Microposit remover 1165 and TechniStrip P1316 seem to produce a much cleaner substrate as little or no resist was visible under the optical microscope. It was later found out that stripping resist in several beakers of clean solutions of remover 1165 at 70°C produces the best

resist removal results and thus remover 1165 was used to strip the resist for realisation of the device.

Although the optimal resist stripper solution was used, resist residues were occasionally observed on graphene at the end of the device fabrication if the resist stripping time was not sufficient. Figure 3.13 compares two suspended graphene devices where resist was stripped in Microposit Remover 1165 for 10 minutes and 1 hour. Clear traces of polymer residues can be observed at the edge of the suspended graphene with the resist stripping time being 10 minutes. These residues may have been the result of resist crosslinking in the graphene patterning step and longer resist stripping times are required for better resist removal results.

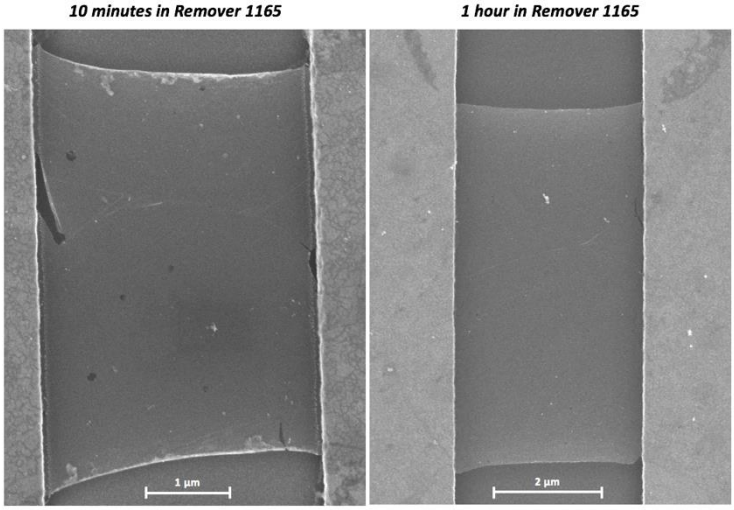

Figure 3.13: Resist residues in two finished devices where resist was stripped in Microposit Remover 1165 for 10 minutes and 1 hour. Clear chunks of polymer residues can be seen at the edge of the suspended graphene beam on the left.

To more efficiently remove resist residues, various methods such as thermal annealing and current annealing can be employed [74] [75]. Thermal annealing was shown to cause the diffusion of gold into the underlying oxide and damage the graphene-Au contact [54]. A discussion on how current annealing was used to remove resist residues and enhance graphene channel resistance will be given in 4.1.

3.2.5.3 Issues Encountered in Releasing Graphene by Etching the Underlying Oxide with Vapour HF

Releasing graphene by etching the underlying oxide with vapour HF has appeared to be a viable approach to make suspended graphene devices and avoid the free-moving graphene sticking to the substrate by surface tension forces [76]. The vapour HF etching apparatus which was available at CMi and which was used in this thesis is Idonus HF VPE-100. The vapour HF etching mechanism employed by this apparatus involves allowing vapour HF, which

evaporates at room temperature, evaporate at defined temperatures from a chamber and reach the substrate clamped on a holder facing down the chamber. The HF vapour phase etch of SiO_2 starts instantaneously.

A thin level of water film on the substrate, which is both the product and catalyst of the etching reaction, must be controlled for efficient etching of the oxide with vapour HF [77]. Too little water slows down the etching process and too much water presents a risk of collapsing the suspended graphene. The operating temperature was chosen to be 60°C, which is the maximum allowed temperature for better etching control and lower risk of introducing too much water on the substrate. Temperature higher than 60°C would lead to the vanishing of the thin water film on the substrate and hinder the etching process.

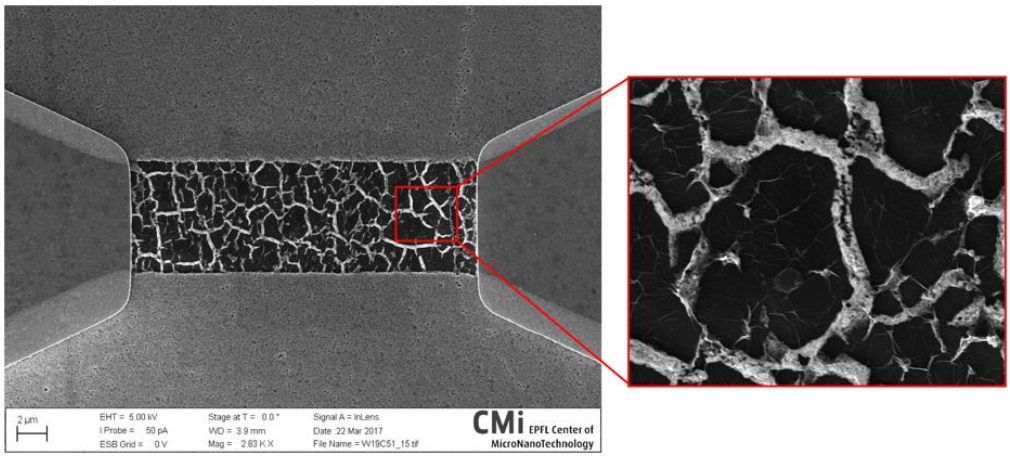

Figure 3.14: Result of graphene release with vapour HF. The uniformity in the etching rate and water presence are thought to be the reason for the graphene beam being broken into pieces.

Figure 3.14 shows the SEM picture of a graphene beam after the suspension step with vapour HF etching. The beam was stuck down to the substrate and broken into pieces. This is attributed to the non-uniformity in the vapour HF etching of oxide and the presence of water during the etching process. Even though the highest allowed temperature at 60°C was imposed, the ineffective clamping of the chip to the holder may have prevented the substrate to be heated to the desired temperature. Besides, the random distribution of the HF vapour which evaporates from the chamber at ambient pressure impedes the uniform oxide etching. Such little control of temperature and pressure within the machine chamber renders this vapour HF etching method unreliable.

3.2.5.4 Issues Encountered during Graphene Release with BHF Wet Etching and CPD

Due to the problems associated with vapour HF etching discussed in the previous section, a graphene release approach which combines oxide etching with BHF and critical point

drying (hereinafter referred to as "BOE+CPD") was adopted. Critical point drying is a well-established method for suspending microstructures by wet etching in M/NEMS. As the liquid in the post-etch liquid solution dries, the surface tension acts to pull down and collapse the suspended structures. In CPD, the liquid is brought to a supercritical state at high pressure and temperature and then changed to the gas state. As the boundary between liquid and gas ceases to exist at the supercritical point, the surface tension induced collapse of structures is avoided. The common fluids suitable for CPD is carbon dioxide (CO_2) which achieves its supercritical point state at 1072 psi and 31°C. CO_2 CPD is employed in this thesis.

The sample is immersed in a solution of BHF 7:1 for etching the underlying oxide and then rinsed carefully in water. The water is then replaced with ethanol before CPD (Automegasamdri®-915B, Series B) is carried out. Since water is not readily miscible with CO_2, it must be replaced with ethanol which is miscible with both water and CO_2. Figure 3.15 summarises the BOE+CPD release process of graphene. The details of each step are provided in Appendix A. Many problems were faced during the BOE+CPD implementation. These issues and how they were addressed are detailed in the following paragraphs.

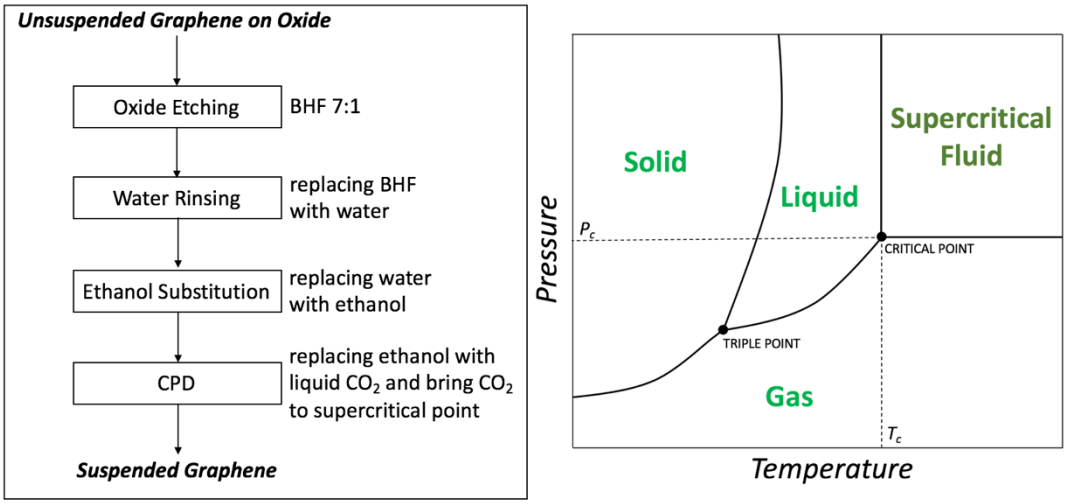

Figure 3.15: (left) Employed BOE+CPD release process of graphene, (right) pressure/temperature phase diagram indicating the achievable supercritical fluid state at temperature T_c and pressure P_c.

Sample exposure to air

The first and most serious problem associated with BOE+CPD is the exposure of samples to air during the process. After the complete etching of the underlying oxide, the hydrophobic silicon surface tends to push the water off the substrate even when the sample is placed horizontally. This induces a large drag force that pulls against the graphene and causes it to collapse.

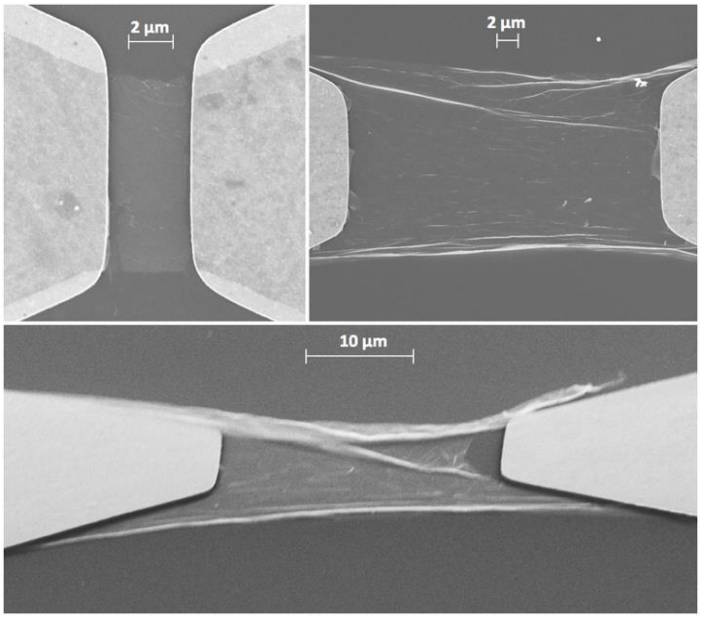

Figure 3.16: BOE+CPD failure: collapse of graphene beams when samples are exposed to air after all the oxide underneath the graphene has been etched in BHF solutions.

Figure 3.16 illustrates the graphene collapse failure when samples are exposed to air after the complete etching of oxide with BHF. Graphene was stuck down to the substrate when the samples were taken out of the BHF bath to the water bath for rinsing, and from the water bath to the ethanol bath. The solution for this graphene collapse problem is to carry out the wet etching of oxide, water rinsing and ethanol substitution in one bath. A dedicated syringe is used to deplete the current solution (i.e., BHF or water) to just above the sample (to avoid the sample being exposed to air) and replace it with next solution (i.e., water or ethanol). The sample is then carefully transferred to the CPD chamber. Care should be taken to have the sample positioned horizontally during this transfer. Since ethanol has much better wettability on Si substrate than water, a sufficiently thick ethanol film will be maintained even when the horizontally oriented sample is exposed to air, thereby eliminating the risk of the sample being directly exposed to air.

Agitation caused by moving the samples

Being one atom thick, the suspended graphene is particularly sensitive to the viscous drag force acting on it when it is moved out of a liquid body and when the liquid body is agitated. Since the sample must eventually be carried from ethanol to the CPD chamber, agitation is inevitable. However, agitation can be kept to a minimum by limiting the liquid to a small volume and moving the sample only one time. Some common failures due to agitation are summarised in Figure 3.17.

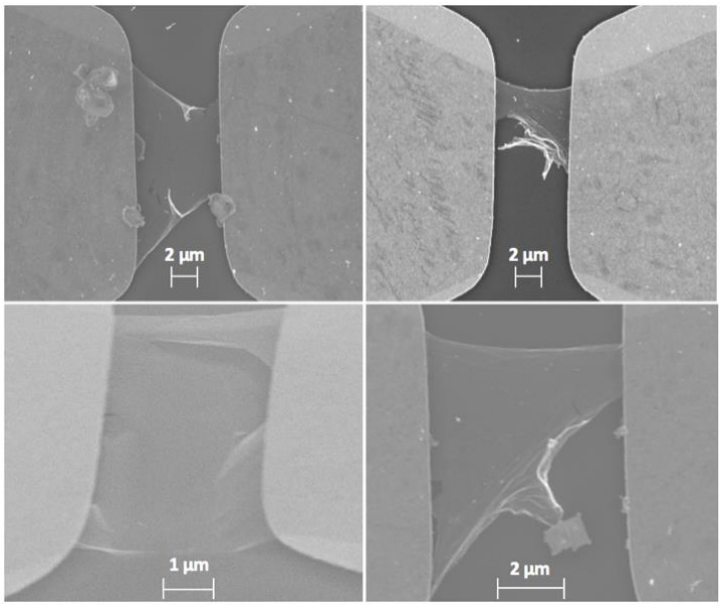

Figure 3.17: BOE+CPD failure: breakage of graphene beams due to agitation induced by moving the samples. The particles that lie next to the devices are etching reaction by-products remaining from insufficient rinsing.

Another source of agitation that could potentially damage the sample is the sudden increase in pressure of the CPD chamber. To start the CPD process, liquid CO_2 is introduced to the chamber through a valve. The value of this valve should be kept at zero and then increased gradually to ensure a gradual increase in pressure in the chamber.

3.2.5.5 Cracks and Holes in Suspended Graphene

A common problem encountered in the suspended graphene beams is the presence of cracks and tears. Some suspended graphene beams with these defects are shown in Figure 3.18.

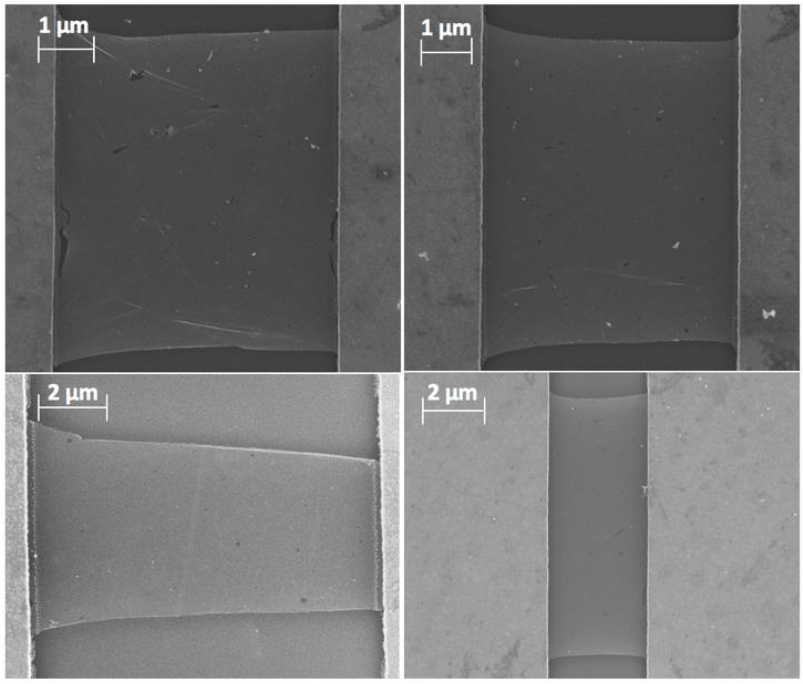

Figure 3.18: Small cracks and holes in suspended graphene, believed to form during resist stripping.

One possible reason for the formation of cracks and tears in the released graphene is the adhesion of graphene to resist used to pattern it. When resist is stripped after graphene patterning, the strong adhesion of resist to graphene could cause local graphene lift-off to occur and thus introduce occasional tears on the graphene membrane. A solution for this problem is to opt for PMMA as the resist to pattern graphene with electron beam lithography since PMMA has been shown to be readily removed from graphene without inducing damage during graphene transfer.

3.2.6 Results and Discussions

Two fabrication runs were carried out in this project. In the first fabrication run, the lengths of the graphene beam were varied across the devices to be 0.5, 3.5, 6.5, 8.5, 13.5, 18.5, 28.5, 38.5, 48.5, 73.5, 98.5 μm, while the device widths were kept the same at 6.5 μm. The error associated with these dimensional values is around 0.5 μm. Graphene suspension was found to be possible only for devices with lengths of 3.5 and 6.5 μm. Graphene beams with lengths equal or greater than 8.5 μm have much smaller stiffness and were easily stuck down to the substrate by the viscous drag forces induced by even a small level of agitation. These dimensions, however, provided a tool to quantify the sheet resistance of the unsuspended graphene. This will be discussed in 4.1.1. The yield for this fabrication run is less than 10%.

Considering the small yield in the first fabrication run, the second fabrication run was carried out with the widths and lengths of the graphene clamped-clamped beams varied from 2.5 to 8.5 μm and from 0.5 to 7.5 μm, respectively. The same chip area of 10×10 mm is more densely packed with devices. The total number of source/drain electrode pairs on a single chip in this fabrication run was increased to 640 compared to 336 in the first fabrication run. The number of produced devices is less than 640, though, since the devices with suspended graphene beams are only located in the region covered by graphene transferred on the chip. The yield of this fabrication run is greater than 80%. Table 2 summarises the designed widths and lengths of the graphene beams in the second fabrication run and highlights the combinations of widths and lengths that yielded suspended devices. All the dimensions reported above are around 1.5 μm smaller than the designed dimensions due to overdose in lithography exposure. The designed dimensions are provided in Appendix B.

Table 2: Widths and lengths of suspended graphene beams from the 2nd fabrication run. The tick marks indicate the width and length combinations that yielded suspended beams.

	W = 2.5 µm	**W = 4.5 µm**	**W = 6.5 µm**	**W = 8.5 µm**
L = 0.5 µm				
L = 1.5 µm	√	√	√	√
L = 2.5 µm	√	√	√	√
L = 3.5 µm	√	√	√	√
L = 4.5 µm	√	√	√	√
L = 5.5 µm	√	√	√	√
L = 6.5 µm	√	√	√	√
L = 7.5 µm	√	√	√	√

The SEM image of a suspended graphene beam from the first fabrication is presented in Figure 3.19. Contaminants due resist residues and etching reaction by-products are visible. Small holes can be observed on the suspended graphene. As discussed, due to the strong adhesion between photoresist and graphene, these holes may have formed during resist stripping. A certain degree of buckling can be seen in the graphene and is attributed to the compressive residual stress existing in the graphene prior to suspension.

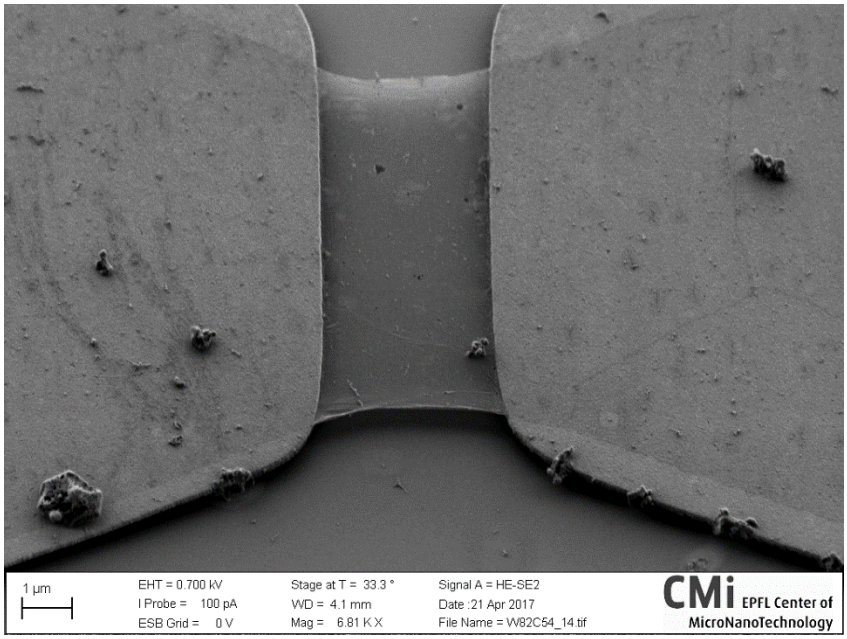

Figure 3.19: Suspended graphene beam from the first fabrication run with width of 8.5 µm and length of 3.5 µm. A small degree of buckling is observed at the edge of the suspended graphene and is attributed to the compressive stress existing in the graphene prior to suspension. The particles seen on the gold pads and graphene are resist residues and by-products of the etching reactions.

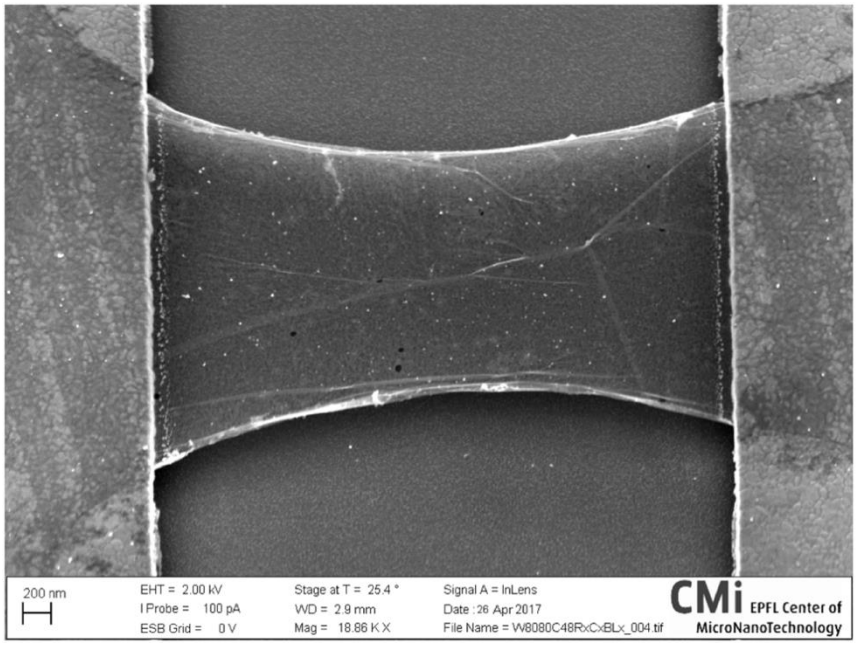

Figure 3.20: Suspended graphene beam from the second fabrication run with width of 2.5 µm and length of 4.5 µm. Small holes formed during resist stripping and multilayer patches (a defect typical in CVD graphene) can be observed. Localised contaminants are visible. The buckling is due to compressive stress existing in the graphene prior to suspension.

Figure 3.20 shows the SEM image of a suspended graphene beam from the second fabrication run. With the higher length/width ratio, this graphene beam exhibits a higher level of buckling than the one shown in Figure 3.19. Again, small holes and localised resist residue contaminants can be observed in the form of scattered white spots.

All in all, the implementation of optimised graphene transfer and device fabrication strategies has resulted in a large yield of suspended graphene beams with different aspect ratios. The wet transfer of CVD graphene onto desired substrates was perfected by utilising a small thickness of supporting PMMA layer. The transferred graphene was efficiently patterned by an optimal combination of photolithography and O_2 plasma etching. Finally, the graphene was successfully released by wet etching and critical point drying. The issues encountered during the fabrication processes were appropriately analysed and tackled. A certain degree of polymer contaminants was observed in the finished devices. These contaminants are most probably the remaining polymer residues that had not been removed during the resist stripping step owing to the strong adhesion between photoresist and graphene. Due to the atomically thin nature of graphene, even a very small amount of contamination could affect its properties. While 3.2.2 points out that the deterioration in graphene's quality by resist residues can be uniquely captured in its Raman spectrum, the electrical characterisation of the fabricated devices in 4.1 shows how graphene's transport properties are greatly altered by these residues.

Chapter 4

Device Characterisation

4.1 Electrical Characterisation

The goal of this section is to provide the results of the electrical measurements performed to characterise the fabricated devices. The devices' electrical resistances were measured and compared to derive graphene channel sheet resistances and gold-graphene contact resistances for both unsuspended and suspended graphene. These values were then benchmarked against those found in literature. The outcome of the suspended graphene's electrical conductance measurements with varied gate voltage will also be presented.

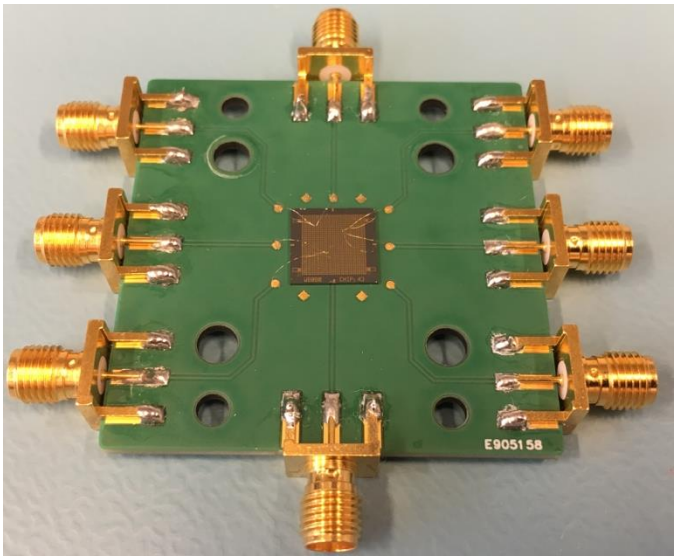

Figure 4.1: Customised PCB with mounted chip having devices wire-bonded for electrical and resonance measurements in vacuum.

The device's electrical properties were measured with an I-V method. A voltage is applied across the device's source and drain electrodes. The source-drain current is measured to deduce the resistance of the device. The graphene's gate-dependent conductance is investigated by monitoring the device's conductance (i.e., the ratio of source-drain current to source-drain voltage) with respect to different values of gate voltage. All measurements to characterise the graphene sheet resistance and graphene-gold contact resistivity were

performed in ambient environment with a probe station and the Hewlett Packard's Precision Semiconductor Parameter Analyser 4156A (HP456A). Graphene's gate-dependent conductance measurements were carried out in vacuum with the chip mounted onto a customised printed circuit board (PCB) and the respective devices wire-bonded to appropriate metal electrode pads located on the PCB (Figure 4.1).

4.1.1 Measurements of Graphene-Gold Contact Resistance and Graphene Channel Sheet Resistance

One of the most common approaches to characterising the graphene-metal ohmic contact is to employ the so-called transmission line method (TLM) for measuring the graphene-metal specific contact resistivity (ρ_c) [78] [79] [80] [81]. In a typical TLM measurement, the total resistance of the graphene devices, which consists of the graphene channel resistance and the graphene-metal contact resistance, is plotted against a wide range of graphene channel lengths.

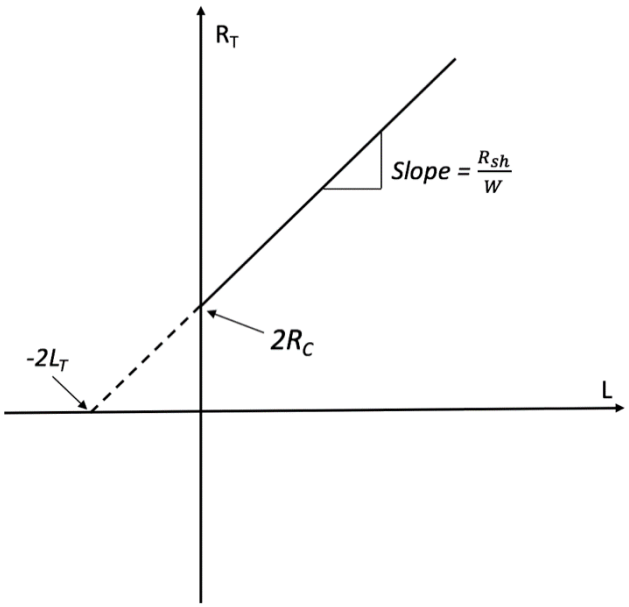

Figure 4.2: Transmission line method to determine the graphene-metal specific contact resistivity and the sheet resistance of the channel graphene, adapted from [94]*. The total resistance is plotted against the length of the graphene channel. The slope of the resistance linear curve is the ratio of channel graphene sheet resistance R_{sh} to the graphene channel width W. The y- and x- intercepts represent the graphene-metal contact resistance R_c and the transfer length L_T.*

Figure 4.2 shows a typical plot of the total resistance (R_T) of the graphene-gold contact and the graphene channel with respect to different separation distances L between the two contacts (i.e., lengths of the graphene channel). The slope of the resistance line gives information about the sheet resistance of graphene R_{sh} for a known value of the channel width W. The intersections of the resistance line to the y and x axes are two times the contact

resistance and transfer length L_T, with L_T being the length that electrons travel across the metal-graphene interface before going into graphene or metal. ρ_c is given by the following formula assuming the contact length (L_c) is much greater than L_T [82]:

$$\rho_c = R_c \times W \times L_T \tag{5}$$

where R_c is the graphene-metal contact resistance for one contact.

The devices with unsuspended graphene fabricated in the first fabrication run were used to measure the specific contact resistivity of the graphene-Au contact and the channel sheet resistance of the unsuspended graphene. As the yield of the second fabrication run was much higher, the devices with suspended graphene fabricated in this run were used to derive the sheet resistance of suspended graphene.

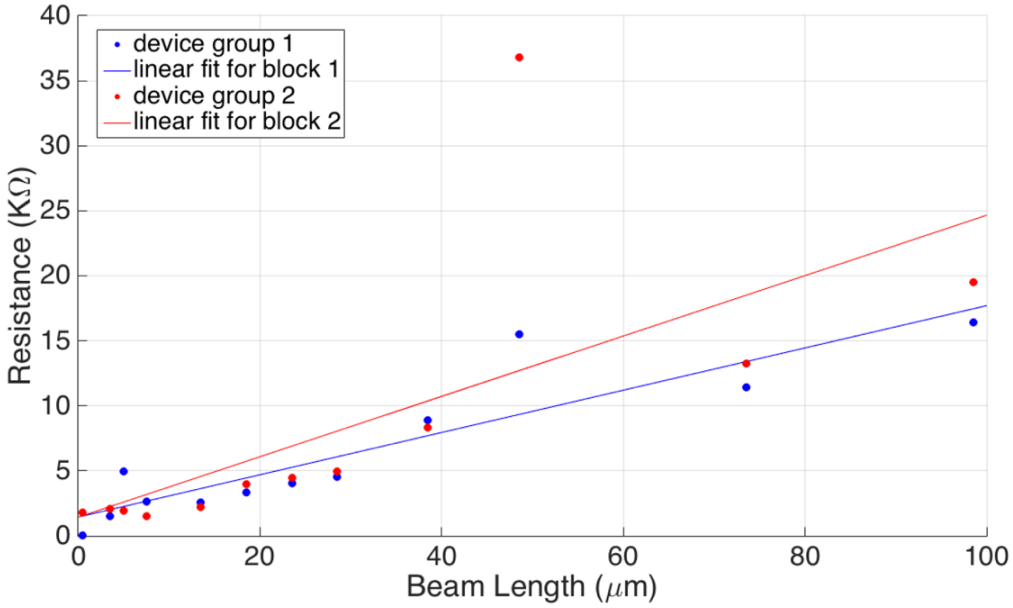

Figure 4.3: Plots of total resistances of devices with unsuspended graphene beams of the same width and different lengths for 2 device groups. The width is kept the same at 6.5 μm whereas the length is swept from 0.5 to 98.5 μm.

Figure 4.3 shows the scatter plots of the total resistances of devices with unsuspended graphene with respect to graphene channel lengths from 0.5 to 98.5 μm for 2 groups of devices. All these devices have the same channel width of 6.5 μm. A linear fit was imposed for the device resistances in each group. The graphene's quality in all the devices within a single group varies due to resist residues and damage induced by resist stripping. This explains the deviation in the resistance of the devices with length of 48.5 μm from the linear trend in both device groups. Table 3 lists the calculated contact resistance, transfer length, graphene channel sheet resistance and specific contact resistivity corresponding to the TLM measurements in each of the two investigated device groups. The differences in values of the graphene-gold specific

contact resistivity can be attributed to the random defects in graphene as the result of resist stripping. These defects cause significant changes in resistance of some devices from the intrinsic values. The presence of defects such as holes and cracks in graphene due to resist stripping is discussed in 3.2.5.5.

Table 3: Results of TLM measurements carried out on devices with unsuspended graphene from the first fabrication run.

	Contact resistance	Transfer length	Graphene channel sheet resistance	Specific contact resistivity
Group 1	575 Ω	3.50 µm	1,377 Ω/□	16,100 Ω.µm^2
Group 2	525 Ω	2.06 µm	1,972 Ω/□	8,652 Ω.µm^2

The metal-graphene contact resistivity reported in literature varied significantly with the best reported value being 1000 Ω.µm^2 for single layer exfoliated graphene [79]. The metal-graphene contact resistivity also differs among different reports although it was recently demonstrated with both transmission line and four-probe method that this value is around 10,000 Ω.µm^2 for gold-graphene contact [83]. These variations are attributed to the different fabrication processes employed to fabricate the graphene devices and resist residues and defects introduced to graphene during the fabrication.

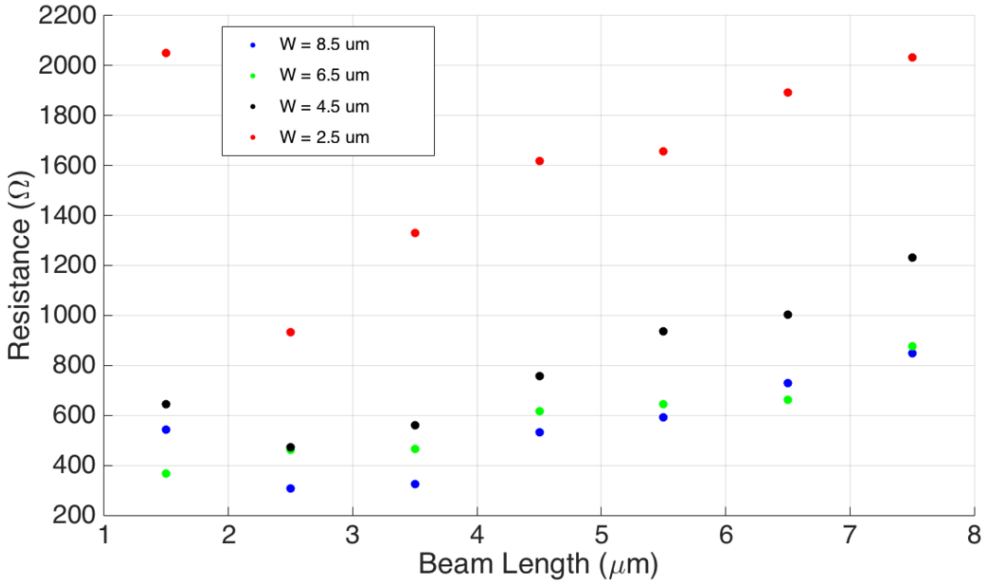

Figure 4.4: Resistance measurements for devices with suspended graphene beams of different widths and lengths from the 2nd fabrication run. The widths are from 2.5 to 8.5 µm while the lengths are from 1.5 µm to 7.5 µm.

Figure 4.4 presents the resistance measurement results for the devices with suspended graphene beams of different lengths and different widths in the second fabrication run. The length was varied from 1.5 µm to 7.5 µm while the width was varied from 2.5 µm to 8.5 µm. A clear trend can be observed where the resistances of the devices of the same width increase with increasing lengths and the resistances of the devices of the same length decrease with increasing widths. However, some exceptions occur for beam lengths of 1.5 µm ad 6.5 µm, where an increase in the width of a suspended graphene beam of the same length does not always correspond to an increase in the device resistance. This is due to the variation in suspended graphene quality which leads to inconsistency in the graphene sheet resistance.

Since the linear fit for the resistances of graphene beams of width 6.5 µm has the largest correlation coefficient (0.92) among the different graphene widths shown Figure 4.4, this linear fit was chosen to calculate the sheet resistance of the suspended graphene with the TLM method, as depicted in Figure 4.5. The slope of the fit is the ratio of the suspended graphene's sheet resistance to the graphene beam width. The sheet resistance of the suspended graphene is thus calculated to be ~500 Ω/□.

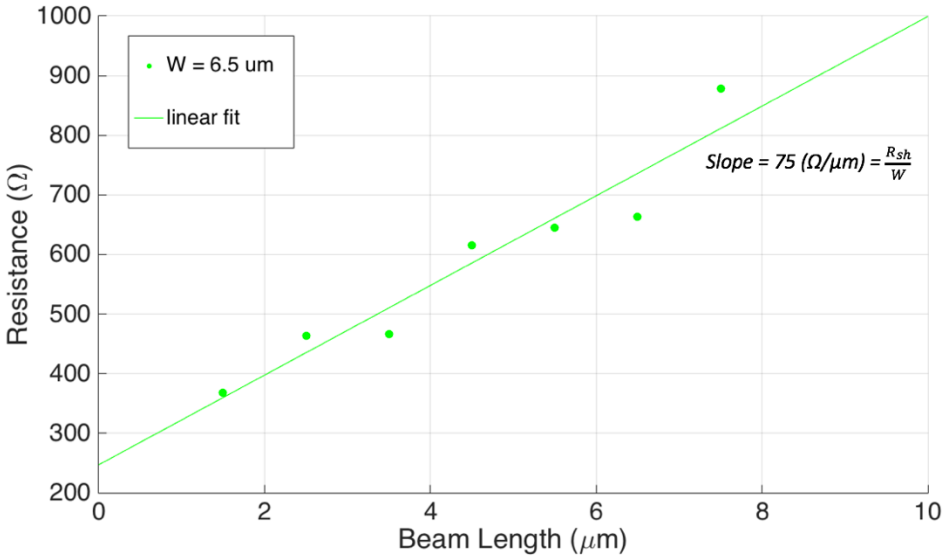

Figure 4.5: Linear fit for resistances of devices with graphene width of 6.5 µm. The correlation factor is 0.92 and largest among the graphene widths investigated. The graphene sheet resistance is found to be ~500 Ω/□.

Graphene has long been regarded as the ideal candidate to replace indium tin oxide (ITO) films as an ideal transparent conducting electrode material. This is due to its superior flexibility, good electrical mobility and high optical transparency. However, while the intrinsic graphene resistance has been demonstrated to be as low as 30 Ω/□, the sheet resistance of single-layer CVD grown graphene is significantly higher [11] [84]. Several reports have

demonstrated stacking several monolayer graphene produces films with low sheet resistance while still maintaining a good optical transparency.

Table 4 summarises the reported sheet resistance values of suspended and unsuspended graphene of one and multiple layers. The graphene's sheet resistance varies greatly among different studies owing to different graphene production, transfer and treatment processes. The general trend is that increasing the number of graphene layers significantly enhances the sheet resistance. Interestingly, there has been little research conducted on comparing the sheet resistances of suspended and unsuspended graphene, although it has been shown that suspending graphene dramatically increases the electronic mobility in graphene [85]. Ref. [43] has pointed out that suspending multi-layer graphene significantly reduces the sheet resistance (from 1250 Ω/□ to 10 Ω/□). The suspended graphene in our work also exhibits a much lower sheet resistance compared to the unsuspended one (500 Ω/□ compared to 1500 Ω/□). A potential reason for the decrease in the sheet resistance in suspended graphene is the decrease in substrate induced scattering, although other factors contributing to the graphene conductivity such as defects and impurities should be considered for more accurate comparison [43].

Table 4: Sheet resistance values of single- and multi- layer unsuspended and suspended graphene reported in literature.

Reference	***Graphene type & substrate***	***Number of layers***	***Graphene sheet resistance (Ω/□)***
[86]	Exfoliated graphene on glass	1	400
		10 nm thick multi-layer	10
[59]	CVD graphene on PDMS	6-10	280
[87]	CVD graphene on glass	1	2100
		4	350
[88]	CVD graphene on PDMS	1-3	510
		8-9	280
[55]	CVD graphene on Polyethylene terephthalate (PET)	4	30
[43]	CVD graphene on silicon nitride (SiN)	7	1250
	Suspended CVD graphene	7	10
Our work	CVD graphene on SiO_2	1	~ **1500**
	Suspended CVD graphene	1	~ **500**

4.1.2 Measurement of Graphene Conductance with respect to Gate Voltage

The most fundamental electrical property of graphene is its bipolar field effect transistor (FET) behaviour, where the graphene's electrical conductance is modulated by nearby electrostatic gating. This gate effect in graphene is possible because of the gate voltage's ability to modulate the density and polarity of charge carriers in graphene [89]. Ideally, the conductivity profile is V-shaped with the minimum conductivity occurring at the minimum conductivity point $V_{g,min}$ (i.e., charge neutrality point or Dirac point) where graphene is un-doped with nominal zero charge. Graphene is doped with holes for $V_g < V_{g,min}$ and with electrons for $V_g > V_{g,min}$. Although $V_{g,min}$ equals zero gate voltage for perfect graphene, due to impurities and defects introduced during the fabrication process, $V_{g,min}$ often deviates from $V_g = 0$. How far $V_{g,min}$ is from $V_g = 0$ could be used as an indicator to assess the quality of the fabricated graphene.

The FET behaviour of graphene was investigated for both suspended and unsuspended graphene beams. While the thermally conductive path provided by SiO_2 substrate enables the electrical transport measurement of unsuspended graphene with a large source-drain voltage V_{sd}, the thermal isolation of graphene in suspended graphene implies V_{sd} must be lower to prevent the ohmic heating induced changes in the device's conductance. The transport properties of unsuspended graphene can be studied with a larger range of gate voltage V_g. This is because the SiO_2 substrate provides the mechanical support for unsuspended graphene against the electrostatic force which tends to pull suspended graphene into electrical contact with the highly doped Si.

Figure 4.6 shows the source-drain current (I_d) curves with respect to gate voltage from -20 to 20 volts (V) for three separate measurements on an unsuspended graphene beam. A clear trend is observed with I_d decreasing with increasing gate voltage V_g. The conductance curve is shifted upward, suggesting the current-induced desorption of contaminant molecules which increases graphene's conductance. The downward conductance profile indicates that the graphene is p-doped and $V_{g,min}$ has been shifted to a high positive gate voltage. This significant positive shift in $V_{g,min}$ is attributed to graphene being contaminated by resist residues during the graphene transfer and device fabrication. Polymer residues have been reported to cause positive shifts in $V_{g,min}$ to voltages as large as 100 V [90].

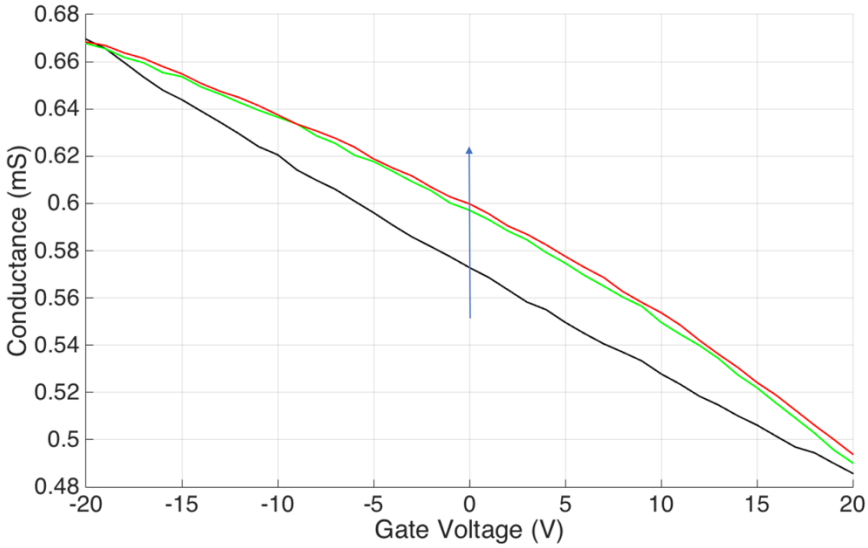

Figure 4.6: Conductance vs. gate voltage curves for three separate measurements on an unsuspended graphene beam having width of 2.5 µm and length of 3.5 µm. V_{sd} is 1 V. The blue arrow indicates the order of the measurements. The graphene is p-doped with the minimum conductivity point being shifted towards a voltage larger than 20 V.

The contact between suspended graphene and the underneath Si gate electrode at large gate voltages can be detected by monitoring the current in the gate terminal (i.e., gate current I_g). Figure 4.7 presents a gate current measurement for a range of gate voltage. Suspended graphene beams with higher width/length ratios are expected to have greater stiffness against the gate voltage induced electrostatic force and thus facilitate gate effect measurements with a larger gate voltage range.

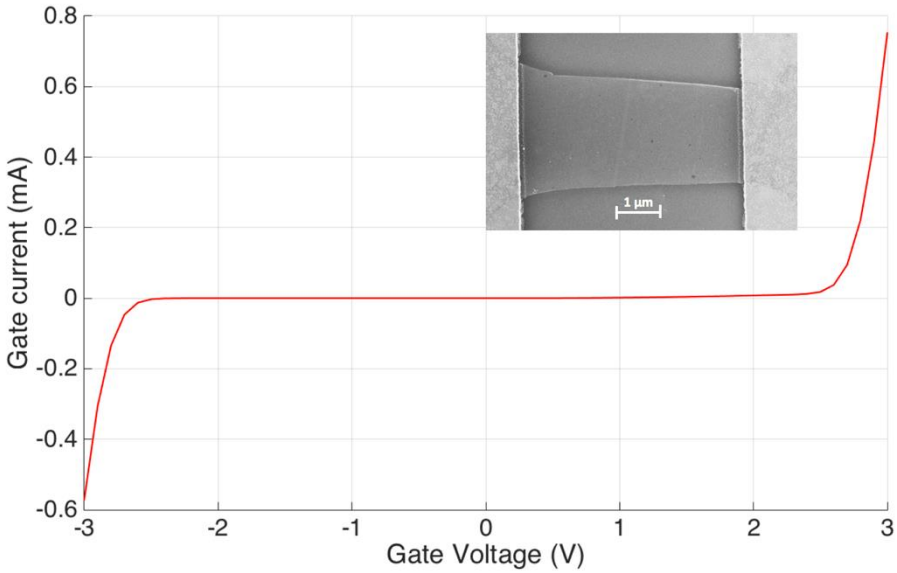

Figure 4.7: Gate current vs. gate voltage graph for a suspended graphene beam having length of 5.5 µm and width of 2.5 µm (inset). V_{sd} is 0.2 V. The surge in I_g for $|V_{sd}| \geq 2.5$ V means the suspended graphene beam starts touching the gate electrode at $|V_{sd}| \geq 2.5$ V.

The transport properties of suspended graphene were studied with I_g monitored to avoid suspended graphene touching and making electrical contact with the gate electrode. Significant improvement in the FET behaviour compared to unsuspended graphene was observed. Figure 4.8 shows the conductance versus gate voltage curve for a suspended graphene beam. The minimum conductivity point $V_{g,min}$ can be seen shifted towards a voltage close to 0 V. V_{sd} was chosen to be 0.1 V to limit the Ohmic heating of graphene during the measurements as thermally induced changes in graphene's resistance could mask its FET behaviour. The conductance profile is shifted upward after each measurement as the current-induced desorption of some contaminant molecules enhances the graphene's conductivity. However, little gate effects are observed for $V_g > 0$ owing to the graphene being p-doped with resist contaminants.

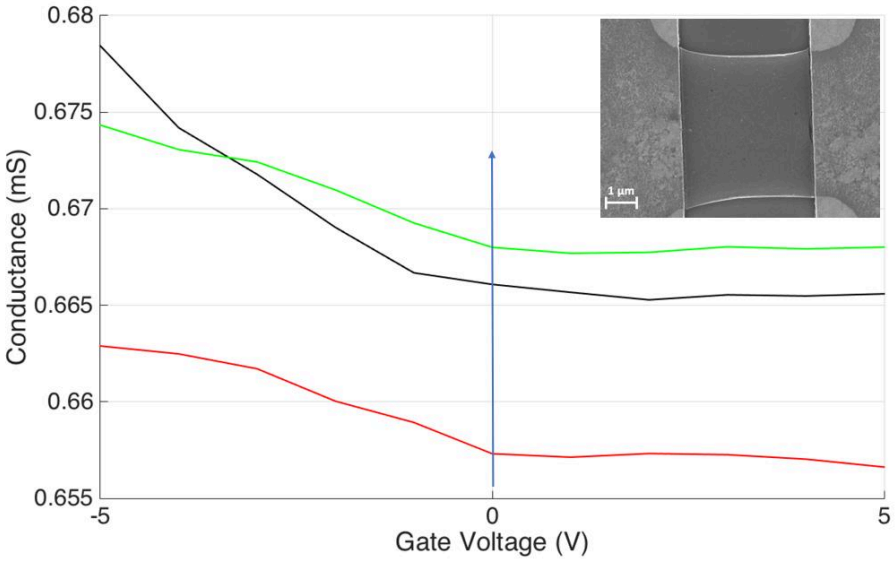

Figure 4.8: Conductance vs. gate voltage curves for three separate measurements on a suspended graphene beam having width of 4.5 µm and length of 4.5 µm (inset). The source-drain voltage V_{sd} is 0.1 V. The blue arrow indicates the order of the measurements. $V_{g,min}$ can be seen close to $V_g = 0$ V. Weak gate effect is observed for $V_g > 0$.

Several graphene cleaning methods such as thermal annealing and current annealing can be employed to recover graphene's intrinsic transport properties. Thermal annealing at several hundreds of degrees Celsius in ultrahigh vacuum or in argon/helium environment has been demonstrated to remove resist contaminants [74]. However, thermal annealing was shown to cause the diffusion of gold into the oxide insulating layer and has not been tried in this thesis. Current annealing has been reported as an effective method to supress contamination in graphene by electro-migration and Joules heating [75]. The power dissipation as large as 20 mW over a small graphene area of few μm^2 has been shown to induce sufficient Joule heating

to cause contaminant nanoparticles to undergo evaporation and sublimation. The upward shifting of the graphene's conductance profile in Figure 4.7 and Figure 4.8 implies the effectiveness of current annealing in cleaning graphene.

The electrical properties of graphene in the fabricated devices have been exhaustively characterised. The graphene's sheet resistance and graphene-gold specific contact resistivity were measured, showing good agreement with the reported values in literature. A significant increase in the sheet resistance was observed upon removing the underlying SiO_2 substrate. The gate-dependent conductance of both unsuspended and suspended graphene beams was confirmed and was shown to improve with current annealing although the complete removal of resist residues is required to recover graphene's intrinsic transport properties. The good electrical characteristics suggests the good quality of graphene in the fabricated device.

Chapter 5

Conclusion and Future Works

5.1 Conclusion

The successful demonstration of a cost-efficient, reproducible and scalable fabrication approach of 2D material based resonators has been achieved in this thesis. Single layer graphene grown by chemical vapour deposition on copper foils was transferred using an optimised wet transfer process on SiO_2/Si substrate with pre-patterned source/drain gold electrodes. The electrode substrates were fabricated on the wafer scale thus greatly reducing the number of fabrication steps. Graphene was transferred on these substrates and optimally patterned with photolithography and O_2 plasma etching. Graphene was suspended by etching the underlying oxide in BHF and critical point drying. Various dimensions of the clamped-clamped suspended graphene ranging from 1.5 μm to 7.5 μm in length and from 2.5 μm to 8.5 μm in width were obtained, facilitating investigation of graphene sheet resistance with the transmission line method.

Electrical measurements of the post-fabrication graphene-gold contact resistivity, graphene's electrical sheet resistance and transport properties were carried out to characterise the graphene's quality. Transmission line measurements were employed to calculate the graphene's sheet resistance and the graphene-gold specific contact resistivity. The sheet resistance was found to be 1500 Ω/□ and 500 Ω/□ for unsuspended graphene and suspended graphene respectively, implying the increase in graphene's mobility by eliminating the SiO_2 substrate. The graphene-gold contact resistivity varies quite significantly between 8000 $\Omega.\mu m^2$ and 1600 $\Omega.\mu m^2$. The presence of defects such as cracks and holes is attributed to the strong adhesion between photoresist and graphene which causes local tears in graphene when the resist is stripped. The strong shift of the minimum conductivity point towards large positive voltages indicates the graphene is p-doped due to resist contamination. The elimination of the SiO_2 substrate in suspended graphene was shown to significantly improve the graphene's transport properties with the minimum conductivity point being observed at voltages close to 0 V. The strong bipolar behaviour typical of good-quality graphene in the fabricated device suggests the reliability of the employed fabrication process.

The work accomplished in this thesis presents a great possibility to fabricate 2D material based NEMS resonators on large scales. Although graphene was used as the demonstration of the fabrication procedures, these procedures should be applicable to other 2D materials. As the collection of 2D materials having a diverse range of unique properties not found in their 3D bulk counterparts continues to grow, this holds great promise for the efficient and large-scale fabrication of 2D materials based NEMS resonators for different applications.

5.2 Future Works

The resist residues and resist stripping induced defects can be supressed by employing electron beam lithography to pattern graphene with PMMA being the mask for plasma etching of graphene. E-beam lithography can also produce devices with smaller dimensions, allowing higher resonant frequencies to be realised. Graphene cleaning methods such as thermal annealing and current annealing will be utilised and optimised to eliminate as much as possible the polymer residues and recover the graphene's intrinsic transport properties.

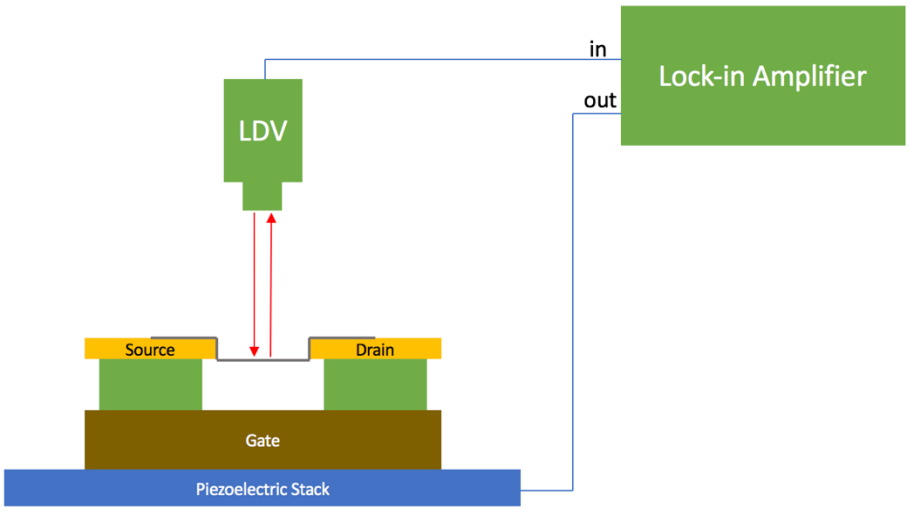

Figure 5.1: Proposed set-up for resonant frequency measurement of the fabricated GNEMS resonators. Lock-amplifier's RF signal f actuates the piezoelectric stack and bring the suspended graphene into motion at f. The graphene's vibration is detected by the LDV which converts the graphene's deflection into an RF signal being fed into the lock-in amplifier. With f being swept within a detection range, the lock-in measurement allows the detection of the device's resonant frequency.

The resonance properties of GNEMS resonator will be measured. As discussed, different optical and electrical transduction techniques for GNEMS resonators have been presented in literature and can be employed to measure the resonant frequency of the fabricated GNEMS resonators. It is important to adopt a transduction technique that allows for an effective read-out of the resonance parameters with the available equipment. Figure 5.1

illustrates a proposed set-up for measuring the GNEMS resonator's resonant frequency. In this setup, the device is rested on top of a piezoelectric transducer. The frequency modulated actuation of the piezoelectric transducer by the lock-in amplifier's output RF signal *f* causes the free-standing graphene to vibrate at *f*. A Laser Doppler Vibrometer (LDV) is employed to monitor the movement of the graphene by sending a laser beam onto the graphene and track another laser beam which is reflected from the graphene. The LDV thus converts the graphene vibration into an output RF signal at the same frequency at which the graphene is actuated (i.e., at *f*). This RF signal is fed as an input signal into the lock-in amplifier, where a lock-in measurement filters out the low frequency component, whose amplitude is proportional to the graphene's vibration amplitude. This way the GNEMS resonator's resonant frequency can be determined by sweeping the *f* within a detection range.

All the above-mentioned future works will be attempted after the delivery of this thesis.

Appendix

A. Fabrication Details

This appendix provides the detailed fabrication procedure to make the graphene resonator device described in the previous chapter. The fabrication was carried out at EPFL's CMi clean room facility and all the tool parameters and recipes to be presented here reflect how the tools are set up and configured in this facility and are reliable at the time of fabrication. The fabrication starts with a ∅100 mm SSP test p-type (0.1- 100 Ω.cm) wafer with 290 nm of wet thermal silicon dioxide (SiO_2) on both sides. Table 5 details the fabrication steps and programs/parameters of the machineries and processes involved.

Table 5: Details of the GNEMS resonator fabrication procedure.

STEP NUMBER	DESCRIPTION	EQUIPMENT	PROGRAMS/PARAMETERS	REMARKS
	GOLD ELECTRODES PATTERNING (WAFER LEVEL)			
	PHOTOLITHOGRAPHY			
1	Spin coating	ACS200	0171_CMi.4in.AZ1512 1um1.onLOR 0um48.	
2	Exposure	MLA150	Light source 405 nm, Defocus 0, dose 70 mJ/cm^2.	
3	Developing	ACS200	0971_CMiDev.4in.AZ152onLOR 0um48.	Developed twice
4	Inspection	Optical Microscope	Check exposure grids and the electrodes patterns.	
	METAL EVAPORATION			
5	Descum	TeplaGIGA	Strip_Low_30s.	
6	Cr/Au evaporation	Alliance-concept EVA 760	Recipe: 450_Cr-Au_50. Parameters: 0.1kÅ of Cr and 1kÅ of Au. Working distance: 450mm.	100 nm of Au on 10 nm of Cr

	LIFT-OFF			
7	Dissolve resist	Plade Solvent	Overnight (16:00 - 7:30) in static 1165 remover bath.	
8	Dissolve resist	Plade Solvent	10 min in ultrasound 1165 remover bath.	
9	Dissolve resist	Plade Solvent	10 min in static 1165 remover bath.	
10	IPA rinse	Plade Solvent	130 s.	
11	Water rinse	Plade Solvent	FRR, 90 s.	
12	Water rinse	Plade Solvent	Frickle, 90 s.	
13	Spin rinse and dry	Semitool Spin Rinser Dryer	Program 1: spin rinse with water and spin dry.	
14	Inspection	Optical Microscope	Check the electrodes patterns.	
	DICING			
15	Spin coating	ACS200	0129_CMi.4in.ECI3027 5um0.HDMS.topEC.	To protect the wafer surface during dicing
16	Oxide strip	Plade Oxide	BHF 7:1, 5 min.	For electrical gate electrodes
18	Dicing	-	-	CMi staff
18	Resist strip	UFT Resist	Standard.	Wafer placed in 2 baths of remover 1165, each for 10 minutes
19	Inspection	Optical Microscope	Check.	
	GRAPHENE TRANSFER (carried out in chemical lab)			
	GRAPHENE PATTERNING (CHIP LEVEL)			

	PHOTOLITHOGRAPHY			
20	Spincoating	SSE SB20	STD-2300rpm.	Resist thickness = 1 µm
21	Exposure	MLA150	Light source 405 nm, exposure 200 mJ/cm^2, Defoc 0.	Alignment is needed
22	Developing	Wetbench	Manual development (beaker) with developer AZ 726 MIF for 1 min and then rinsed with water.	
23	Inspection	Microscope	Check resist patterns and graphene surface.	
	GRAPHENE ETCHING			
24	Oxygen plasma etching	TeplaGIGA	low_2min.	Plasma power = 200W
25	Inspection	Microscope	Check resist patterns and graphene surface.	
	RESIST STRIPPING			
26	Resist strip	Wet bench	Chips placed in 3 clean beakers of remover 1165, each for 10 minutes.	
27	Inspection	Microscope	Check patterned graphene for resist residues.	
	GRAPHENE RELEASE (CHIP LEVEL)			
28	Underlying etching	Wet bench	Chip is placed in one teflon beaker of BHF 7:1 (HF : NH_4F = 12.5 : 87.5%), etched 5 minutes.	300-nm thick oxide is etched
29	Rinsing with water	Wet bench	BHF is depleted and water is introduced with a dedicated syringe. Repeating several times until pH level reaches 7 (checking with pH paper).	200 ml of BHF

30	Replacing water with ethanol	Wet bench	Water is depleted and ethanol 99% is introduced with a dedicated syringe.	500 ml of ethanol is required
31	Critical point drying	Automegasamdri®-915B, Series B	Horizontally oriented sample is transferred into the CPD chamber. Purge time of 10 minutes. Fill valve initially set at zero and then increased to 1.15.	

B. Device Distribution on Chips and Wafers

This section summarises the distributions of chips on a single wafer and of devices on a single chip. As mentioned in 3.2.6, two fabrication runs were carried out with the second run employing more devices on the same chip area and with a smaller range of devices' lengths. Due to the similarities in the devices-on-chip distribution between the two fabrication runs, only the distribution in the second run is presented here. The same chips-on-wafer distribution was implemented for both fabrication runs.

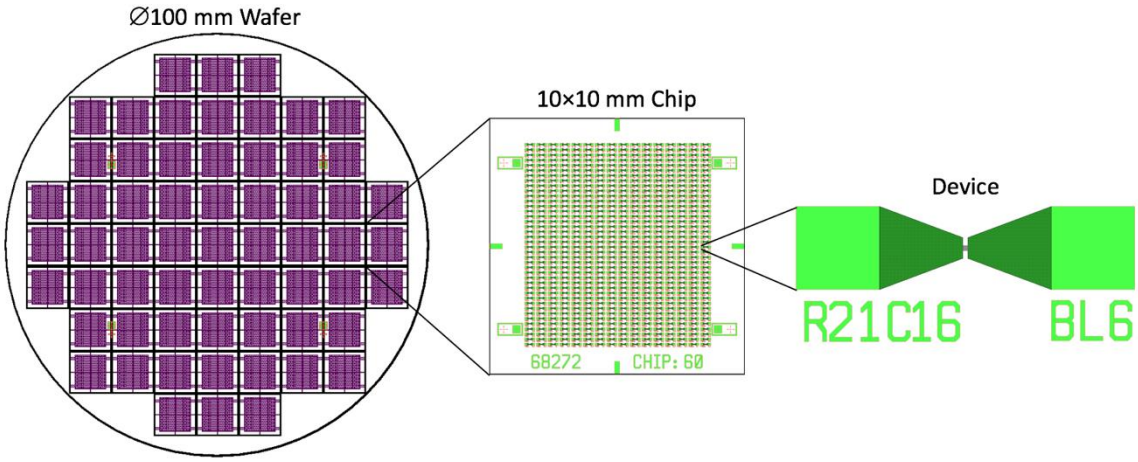

Figure B.1: Chips distribution on wafer and devices distribution on chip. Note that the graphene is transferred and patterned after the chips with source/drain electrodes pairs are produced.

Figure B.1 describes how the chips are distributed on a wafer and how the graphene resonator devices are distributed on a single chip. The graphene seen in the device is for illustrative purposes only. Graphene is transferred, patterned and released on the chips with source/drain electrodes pairs. Figure B.2 presents the chip layout where devices of different graphene beam widths and lengths are distributed across the substrate. The devices of designed

length from 2 to 9 µm are organised into groups of different lengths. These groups are distributed across the chip for ease of monitoring the devices with suspended graphene of different dimensions. Note that these designed length and width values are slightly greater the real values due to slight overdose during lithography exposure. The real lengths and widths of the devices are given in 3.2.6.

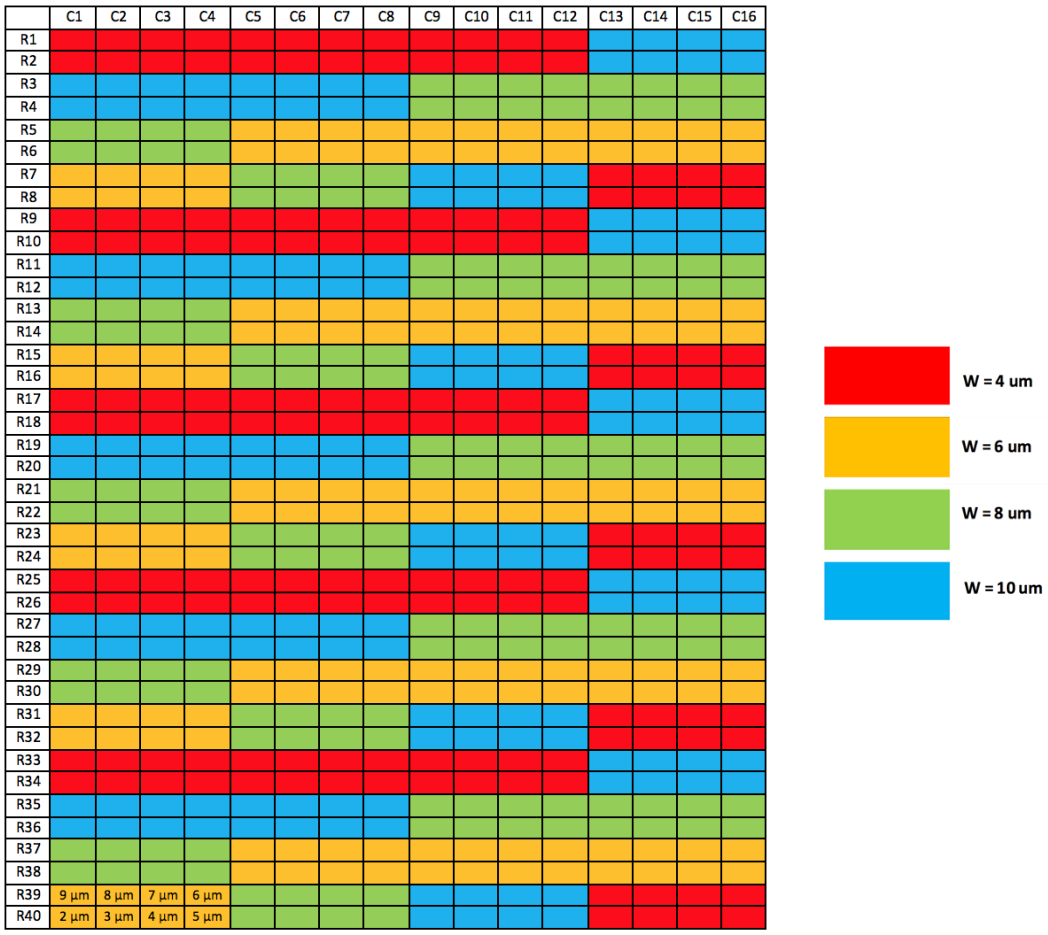

Figure B.2: Chip layout. Devices of different designed graphene beam lengths (BL) from 2 µm and 9 µm are grouped together. These groups of devices have different designed widths (W) and are swept across the chip for ease of monitoring successfully fabricated devices.

C. Matlab programs for measuring the devices' electrical properties with Hewlett Packard's Precision Semiconductor Parameter Analyser 4156A (HP456A)

The following Matlab program was used to measure the devices' resistances with HP456A.

```
function [V_SD,I_SD,GateVoltage,R, I_G] =
HP4156AFET(SweepStart,SweepStop,SweepStep,GateVoltage,filename)
%%%%% How to use the code %%%%%%
%1. Connect source, drain and gate of a FET to SMU1, SMU2 and SMU3 respectively
%2. Turn on the HP4156A
%3. Connect computer to HP4156A using USB to GPIB
%4. Run function with desired parameters.

%Clean up before start
%clear all
%close all
%clc

%%%%%%% Naming and setting parameter %%%%%%%
SMU1V = 'VS'; %Source
SMU1I = 'IS'; %Source
SMU2V = 'VD'; %Drain
SMU2I = 'ID'; %Drain
SMU3V = 'VG'; %Gate
SMU3I = 'IG'; %Gate

% Find a GPIB object.
g = instrfind('Type', 'gpib', 'BoardIndex', 0, 'PrimaryAddress', 1, 'Tag', '');

% Create the GPIB object if it does not exist
% otherwise use the object that was found.
if isempty(g)
    g = gpib('NI', 0, 1);
else
    fclose(g);
    g = g(1);
end

% Set buffer size
g.InputBufferSize = 50000;                          % Set size of input buffer
g.OutputBufferSize = 50000;                         % Set size of output buffer

% Connect to instrument object, g.
fopen(g);

% Reset to initial setting
fprintf(g,'*RST');

%%%%%%%%%%%%%%%% Set channel properties %%%%%%%%%%%%%%%
% SMU1
fprintf(g,':PAGE:CHAN:SMU1:VNAM "%s"',SMU1V);
fprintf(g,':PAGE:CHAN:SMU1:INAM "%s"',SMU1I);
fprintf(g,':PAGE:CHAN:SMU1:MODE COMM');
fprintf(g,':PAGE:CHAN:SMU1:FUNC CONS');

% SMU2
fprintf(g,':PAGE:CHAN:SMU2:VNAM "%s"',SMU2V);
fprintf(g,':PAGE:CHAN:SMU2:INAM "%s"',SMU2I);
fprintf(g,':PAGE:CHAN:SMU2:MODE V');
```

```
fprintf(g,':PAGE:CHAN:SMU2:FUNC VAR1');

% SMU3
fprintf(g,':PAGE:CHAN:SMU3:VNAM "%s"',SMU3V);
fprintf(g,':PAGE:CHAN:SMU3:INAM "%s"',SMU3I);
fprintf(g,':PAGE:CHAN:SMU3:MODE V');
fprintf(g,':PAGE:CHAN:SMU3:FUNC CONS');

% Clear remaining channels
fprintf(g,':PAGE:CHAN:SMU4:DIS');
fprintf(g,':PAGE:CHAN:VSU1:DIS');
fprintf(g,':PAGE:CHAN:VSU2:DIS');
fprintf(g,':PAGE:CHAN:VMU1:DIS');
fprintf(g,':PAGE:CHAN:VMU2:DIS');

pause(2)

%%%%%%%%%%%%%%%% Set sweep parameters and Gate Voltage %%%%%%%%%%%%%%%%%%
fprintf(g,':PAGE:MEAS:VAR1:START %f V',SweepStart);     % Set sweep start parameter
fprintf(g,':PAGE:MEAS:VAR1:STOP %f V',SweepStop);       % Set sweep start parameter
fprintf(g,':PAGE:MEAS:VAR1:STEP %f V',SweepStep);       % Set step size unit can be
fprintf(g,':PAGE:MEAS:CONS:SMU3 %f V',GateVoltage);     % Set gate voltage unit can

pause(2)

%%%%%%%%%%%%% Set plot details %%%%%%%%%%%%%%%
fprintf(g,':PAGE:DISP:GRAP:Y2:NAME "IG"'); % Plot source drain

%%%%%%%%%%%%%%%% Executes measurement %%%%%%%%%%%%%%%%%%
fprintf(g,':PAGE:SCON:SING');                    % Excute the measurement

query(g, '*OPC?');                               % Wait for measurement to complete

fprintf(g,'DATA? "%s"',SMU2I);                          % Ask for ID data
current = fgets(g);                                     % Get ID data
fprintf(g,'DATA? "%s"',SMU2V);                          % Ask for ID data
voltage = fgets(g);                                     % Get ID data
fprintf(g,'DATA? "%s"',SMU3I);                          % Ask for ID data
IG = fgets(g);                                          % Get ID data

pause(1)

%%%%%%%%% Convert from string to number %%%%%%%%%%%%%%%%%%%%%%%%
V_SD(:,1) = str2num(voltage)';                      % Change from string to number
I_SD(:,1) = str2num(current)';                      % Change from string to number
I_G = str2num(IG)';                                 % Change from string to number

%%%%%%%%%%%%% Autoscaling of the plot on the HP4156A %%%%%%%%%%%%%%%
fprintf(g, ':PAGE:GLISt:GRAPhics:SCALing:AUTO ONCE ')

%%%%%%%%%%%%%% Disconnect from instrument and clean up %%%%%%%%%
fclose(g);
delete(g)
clear g
```

```
figure(1)
plot(V_SD(:,1),I_SD(:,1),'.k')
set(gcf,'color','w');                                    % Remove the gray rim
around of plot
set(gca,'FontSize',14)                                   % Set font size to 14
set(gca,'LineWidth',2)                                   % Set axis line width to 2
xlabel('V_D [V]')                                        % Labeling of x
ylabel('I_D [A]')                                        % Labeling of y

%Calculate the resistance for all values
R(:,1)=V_SD(:,1)./I_SD(:,1);

FileName=[datestr(now, 'yyyymmdd-HHMMSS-'),filename, '_Vd = ',
    num2str(SweepStop),'V', '_Vg = ', num2str(GateVoltage),'V.mat'];

save(FileName);                                          % Store data

end
```

The following Matlab program was used for the measurement of the devices' conductance versus varying gate voltage with HP456A.

```
function [V_G,I_SD,DrainVoltage, I_G] =
HP4156AFETGateSweep(GateStart,GateStop,GateStep,DrainVoltage,DeviceName)
%%%%% How to use the code %%%%%%
%1. Connect source, drain and gate of a FET to SMU1, 2 and 3 respectively
%2. Turn on the HP4156A
%3. Connect computer to HP4156A using USB to GPIB
%4. Run function with wanted parameters.

%%%%%%% Naming and setting parameter
SMU1V = 'VS'; %Source
SMU1I = 'IS'; %Source
SMU2V = 'VD'; %Drain
SMU2I = 'ID'; %Drain
SMU3V = 'VG'; %Gate
SMU3I = 'IG'; %Gate

% Find a GPIB object
g = instrfind('Type', 'gpib', 'BoardIndex', 0, 'PrimaryAddress', 1, 'Tag', '');

% Create the GPIB object if it does not exist
% otherwise use the object that was found
if isempty(g)
    g = gpib('NI', 0, 1);
else
    fclose(g);
```

```
    g = g(1);
end

%Set buffer size
g.InputBufferSize = 50000;                              % Set size of input buffer
g.OutputBufferSize = 50000;                             % Set size of output buffer

% Connect to instrument object, obj1
fopen(g);

%Reset to initial setting
fprintf(g,'*RST');

%%%%%%%%%%%%%%%%% Set channel properties %%%%%%%%%%%%%%%%
% SMU1
fprintf(g,':PAGE:CHAN:SMU1:VNAM "%s"',SMU1V);
fprintf(g,':PAGE:CHAN:SMU1:INAM "%s"',SMU1I);
fprintf(g,':PAGE:CHAN:SMU1:MODE COMM');
fprintf(g,':PAGE:CHAN:SMU1:FUNC CONS');

% SMU2
fprintf(g,':PAGE:CHAN:SMU2:VNAM "%s"',SMU2V);
fprintf(g,':PAGE:CHAN:SMU2:INAM "%s"',SMU2I);
fprintf(g,':PAGE:CHAN:SMU2:MODE V');
fprintf(g,':PAGE:CHAN:SMU2:FUNC CONS');

% SMU3
fprintf(g,':PAGE:CHAN:SMU3:VNAM "%s"',SMU3V);
fprintf(g,':PAGE:CHAN:SMU3:INAM "%s"',SMU3I);
fprintf(g,':PAGE:CHAN:SMU3:MODE V');
fprintf(g,':PAGE:CHAN:SMU3:FUNC VAR1');

% Clear remaining channels
fprintf(g,':PAGE:CHAN:SMU4:DIS');
fprintf(g,':PAGE:CHAN:VSU1:DIS');
fprintf(g,':PAGE:CHAN:VSU2:DIS');
fprintf(g,':PAGE:CHAN:VMU1:DIS');
fprintf(g,':PAGE:CHAN:VMU2:DIS');

pause(1)

%%%%%%%%%%%%%%%%% Set sweep parameters and Gate Voltage %%%%%%%%%%%%%%%%%%%
fprintf(g,':PAGE:MEAS:VAR1:START %f V',GateStart);      % Set sweep start parameter
fprintf(g,':PAGE:MEAS:VAR1:STOP %f V',GateStop);        % Set sweep start parameter
fprintf(g,':PAGE:MEAS:VAR1:STEP %f V',GateStep);        % Set step size unit
fprintf(g,':PAGE:MEAS:CONS:SMU2 %f V',DrainVoltage);    % Set gate voltage
fprintf(g,':PAGE:MEAS:CONS:SMU2:COMP 0.1 A');

fprintf(g, ':PAGE:MEAS:SWE:HTIM 1');                    % Set the hold time [S]
fprintf(g, ':PAGE:MEAS:SWE:DEL 1');                     % Set the delay time [S]
pause(1)

%%%%%%%%%%%% Set plot details %%%%%%%%%%%%%%%
%Set x axis
fprintf(g,':PAGE:DISP:GRAP:X:NAME "VG"');
```

```
%Set y axis
fprintf(g,':PAGE:DISP:GRAP:Y1:NAME "ID"');              % Plot source drain current
as a function of gate voltage
fprintf(g,':PAGE:DISP:GRAP:Y2:NAME "IG"');              % Plot gate current as a
function of gate voltage

%%%%%%%%%%%%%%% Executes measurement %%%%%%%%%%%%%%%%%%
fprintf(g,':PAGE:SCON:SING');                           % Excute the measurement

pause(60)

query(g, '*OPC?');                                  % Wait for measurement to complete

fprintf(g,'DATA? "%s"',SMU2I);                          % Ask for ID data
ISD = fgets(g);                                         % Get ID data
fprintf(g,'DATA? "%s"',SMU3V);                          % Ask for ID data
VG = fgets(g);                                          % Get ID data
fprintf(g,'DATA? "%s"',SMU3I);                          % Ask for ID data
IG = fgets(g);                                          % Get ID data

pause(1)

%%%%%%%%% Convert from string to number %%%%%%%%%%%%%%%%%%%%%%%%
V_G = str2num(VG);                                  % Change from string to number
I_SD = str2num(ISD);                                % Change from string to number
I_G = str2num(IG);                                  % Change from string to number

%%%%%%%%%%%%% Autoscaling of the plot on the HP4156A %%%%%%%%%%%%%%%
fprintf(g, ':PAGE:GLISt:GRAPhics:SCALing:AUTO ONCE ')

%%%%%%%%%%%%%% Disconnect from instrument and clean up %%%%%%%%%
fclose(g);
delete(g)
clear g

plot(V_G,I_SD,'.m')
set(gcf,'color','w');                               % Remove the gray rim around
of plot
set(gca,'FontSize',14)                              % Set fontsize to 12
set(gca,'LineWidth',2.5)                            % Set axis line width to 2
xlabel('V_G [V]')                                   % Labeling of x
ylabel('I_SD [A]')                                  % Labeling of y

FileName=[datestr(now, 'yyyymmdd-HHMMSS-'),DeviceName,'-
',num2str(DrainVoltage),'VD.mat'];
save(FileName,'V_G','I_SD','DrainVoltage','I_G');       % Store data
```

D. L-Edit T-Cell program for parametrising the dimensions of the lithography masks of the GNEMS resonators

The following codes were used to parameterise the lithography mask dimensions for the fabricated GNEMS resonators. L-Edit's parametrisation capability enables the distribution of devices of different dimensions (i.e., widths and lengths) across the chips and wafer.

```
#include <cstdlib>
#include <cmath>
#include <cstring>
#include <cstdio>
#include <string>
#include <time.h>

#define EXCLUDE_LEDIT_LEGACY_UPI
#include <ldata.h>


/* Begin -- Uncomment this block if you are using L-Comp. */
//#include <lcomp.h>
/* End */

/* TODO: Put local functions here. */
void cell_sd_main(void)
{
        int iTmpUpiReturnCode = LUpi_GetReturnCode();
        /* Begin DO NOT EDIT SECTION generated by L-Edit */
        LCell          cellCurrent    = (LCell)LMacro_GetNewTCell();
        double       BL           = LCell_GetParameterAsDouble(cellCurrent, "BL");
        /* End DO NOT EDIT SECTION generated by L-Edit */

        if(LUpi_GetReturnCode())
        {
                LDialog_MsgBox("Error: Tcell failed to read parameters.");
                return;
        }
        LUpi_SetReturnCode(iTmpUpiReturnCode);


        /* Begin -- Uncomment this block if you are using L-Comp. */
        //LC_InitializeStateFromCell(cellCurrent);

        /* End */

        /* TODO: Put local variables here. */
        LCoord BeamLength = BL*1000; /*Convert to microns*/
        const char * ch_BL = LCell_GetParameterValue(cellCurrent, "BL");

        /* TODO: Begin custom generator code.*/
        LFile pFile = LCell_GetFile(cellCurrent);
        LLayer Gate  = LLayer_Find(pFile, "Gate");
        LLayer Graphene = LLayer_Find(pFile, "Graphene");

        //Definition of Source contact
```

```
        LCoord s_xcoord1 = 0;
        LCoord s_ycoord1 = 100000;
        LCoord s_xcoord2 = 100000;
        LCoord s_ycoord2 = 100000;
        LCoord s_xcoord3 = 200000;
        LCoord s_ycoord3 = 62500;
        LCoord s_xcoord4 = 200000;
        LCoord s_ycoord4 = 37500;
        LCoord s_xcoord5 = 100000;
        LCoord s_ycoord5 = 0;
        LCoord s_xcoord6 = 0;
        LCoord s_ycoord6 = 0;
        LPoint s_pt1 = LPoint_Set(s_xcoord1, s_ycoord1);
        LPoint s_pt2 = LPoint_Set(s_xcoord2, s_ycoord2);
        LPoint s_pt3 = LPoint_Set(s_xcoord3, s_ycoord3);
        LPoint s_pt4 = LPoint_Set(s_xcoord4, s_ycoord4);
        LPoint s_pt5 = LPoint_Set(s_xcoord5, s_ycoord5);
        LPoint s_pt6 = LPoint_Set(s_xcoord6, s_ycoord6);
        LPoint arraySource [6] = {s_pt1, s_pt2, s_pt3, s_pt4, s_pt5, s_pt6};


        LPolygon_New(cellCurrent, Gate, arraySource, 6);


        //Definition of Drain contact
        LCoord d_xcoord1 = 200000+BeamLength;
        LCoord d_ycoord1 = 62500;
        LCoord d_xcoord2 = 300000+BeamLength;
        LCoord d_ycoord2 = 100000;
        LCoord d_xcoord3 = 400000+BeamLength;
        LCoord d_ycoord3 = 100000;
        LCoord d_xcoord4 = 400000+BeamLength;
        LCoord d_ycoord4 = 0;
        LCoord d_xcoord5 = 300000+BeamLength;
        LCoord d_ycoord5 = 0;
        LCoord d_xcoord6 = 200000+BeamLength;
        LCoord d_ycoord6 = 37500;

        LPoint d_pt1 = LPoint_Set(d_xcoord1, d_ycoord1);
        LPoint d_pt2 = LPoint_Set(d_xcoord2, d_ycoord2);
        LPoint d_pt3 = LPoint_Set(d_xcoord3, d_ycoord3);
        LPoint d_pt4 = LPoint_Set(d_xcoord4, d_ycoord4);
        LPoint d_pt5 = LPoint_Set(d_xcoord5, d_ycoord5);
        LPoint d_pt6 = LPoint_Set(d_xcoord6, d_ycoord6);
        LPoint arrayDrain [6] = {d_pt1, d_pt2, d_pt3, d_pt4, d_pt5, d_pt6};

        LPolygon_New(cellCurrent, Gate, arrayDrain, 6);

        //Definition of graphene beam
        LCell_MakeLogo(cellCurrent, "BL", 70000, Gate, LFALSE, LFALSE,
LFALSE,300000+BeamLength, -37000, LFALSE, LFALSE, LFALSE, NULL, NULL, NULL, NULL);
   LCell_MakeLogo(cellCurrent, ch_BL,70000 , Gate, LFALSE, LFALSE, LFALSE,
370000+BeamLength, -37000, LFALSE, LFALSE, LFALSE, NULL, NULL, NULL, NULL);

        /* End custom generator code.*/
```

```
}
extern "C" int UPI_Entry_Point(void)
{
cell_sd_main();
return 1;
}
```

References

[1] H. Van Heeren and P. Salomon, “MEMS - Recent Developments, Future Directions,” 2007.

[2] L. G. Villanueva, J. Bausells, and J. Brugger, “Grand Challenge in N/MEMS,” *Front. Mech. Eng.*, vol. 1, no. January, 2016.

[3] M. L. Roukes, “Nanoelectromechanical Systems,” in *Transducers ’01 Eurosensors XV*, 2001.

[4] I. Bargatin, “High-frequency nanomechanical resonators for sensor applications (PhD thesis),” California Institute of Technology, 2008.

[5] O. Brand and H. Baltes, “Micromachined Resonant Sensors - an Overview,” *Sensors Update*, vol. 4, no. 1. pp. 3–51, 1998.

[6] H. Craighead, “Nanoelectromechanical systems,” *Arxiv*, vol. 290, no. 5496, p. 1532, 2000.

[7] K. S. Novoselov, A. K. Geim, S. V Morozov, D. Jiang, Y. Zhang, S. V Dubonos, I. V Grigorieva, and A. A. Firsov, “Electric field effect in atomically thin carbon films.,” *Science*, vol. 306, no. 5696, pp. 666–669, 2004.

[8] D. R. Cooper, B. D’Anjou, N. Ghattamaneni, B. Harack, M. Hilke, A. Horth, N. Majlis, M. Massicotte, L. Vandsburger, E. Whiteway, and V. Yu, “Experimental review of graphene,” vol. 2012, 2011.

[9] A. K. Geim and K. S. Novoselov, “The rise of graphene,” *Nat. Mater.*, vol. 6, no. 3, pp. 183–191, 2007.

[10] M. S. Fuhrer, C. N. Lau, and A. H. MacDonald, “Graphene: Materially Better Carbon,” *MRS Bull.*, vol. 35, no. 4, pp. 289–295, 2010.

[11] J.-H. Chen, C. Jang, S. Xiao, M. Ishigami, and M. S. Fuhrer, “Intrinsic and extrinsic performance limits of graphene devices on SiO2,” *Nat. Nanotechnol.*, vol. 3, no. 4, pp. 206–209, 2008.

[12] C. Lee, X. Wei, J. W. Kysar, and J. Hone, “Measurement of the Elastic Properties and Intrinsic Strength of Monolayer Graphene,” *Science (80-.).*, vol. 321, no. 5887, pp. 385–388, 2008.

[13] A. A. Balandin, S. Ghosh, W. Bao, I. Calizo, D. Teweldebrhan, F. Miao, and C. N. Lau, “Superior thermal conductivity of single-layer graphene,” *Nano Lett.*, vol. 8, no. 3, pp. 902–907, 2008.

[14] F. Bonaccorso, Z. Sun, T. Hasan, and A. C. Ferrari, “Graphene Photonics and Optoelectronics,” vol. 4, no. August, pp. 611–622, 2010.

[15] C.-H. Liu, Y.-C. Chang, T. B. Norris, and Z. Zhong, “Graphene photodetectors with ultra-broadband and high responsivity at room temperature,” *Nat. Nanotechnol.*, vol. 9, no. 4, pp. 273–278, 2014.

[16] K. Watanabe, T. Taniguchi, and H. Kanda, “Direct-bandgap properties and evidence for ultraviolet lasing of hexagonal boron nitride single crystal,” *Nat. Mater.*, vol. 3, no. 6, pp. 404–409, 2004.

[17] A. Pakdel, Y. Bando, and D. Golberg, “Nano boron nitride flatland,” *Chem. Soc. Rev.*, vol. 43, no. 3, pp. 934–959, 2014.

[18] Q. H. Wang, K. Kalantar-Zadeh, A. Kis, J. N. Coleman, and M. S. Strano, “Electronics and optoelectronics of two-dimensional transition metal dichalcogenides,” *Nat. Nanotechnol.*, vol. 7, no. 11, pp. 699–712, 2012.

[19] Y. Liu, N. O. Weiss, X. Duan, H.-C. Cheng, Y. Huang, and X. Duan, “Van der Waals heterostructures and devices,” *Nat. Rev. Mater.*, vol. 1, no. 9, p. 16042, 2016.

[20] K. He, C. Poole, K. F. Mak, and J. Shan, “Experimental demonstration of continuous electronic structure tuning via strain in atomically thin MoS2,” *Nano Lett.*, vol. 13, no. 6, pp. 2931–2936, 2013.

[21] S. Bertolazzi, J. Brivio, and A. Kis, “Stretching and breaking of ultrathin MoS 2,” *ACS Nano*, vol. 5, no. 12, pp. 9703–9709, 2011.

[22] A. Castellanos-Gomez, M. Poot, G. a Steele, H. S. J. van der Zant, N. Agraït, and G. Rubio-Bollinger, “Elastic Properties of Freely Suspended MoS2 Nanosheets.,” *Adv. Mater.*, vol. 24, no. 6, pp. 772–5, 2012.

[23] J. Qiao, X. Kong, Z.-X. Hu, F. Yang, and W. Ji, “High-mobility transport anisotropy and linear dichroism in few-layer black phosphorus,” *Nat. Commun.*, vol. 5, 2014.

[24] Q. Wei and X. Peng, “Superior mechanical flexibility of phosphorene and few-layer black phosphorus,” *Appl. Phys. Lett.*, vol. 104, no. 25, 2014.

[25] J.-W. Jiang and H. S. Park, “Mechanical Properties of Single-Layer Black Phosphorus,” 2014.

[26] S. Z. Butler, S. M. Hollen, L. Cao, Y. Cui, J. A. Gupta, H. R. Gutierrez, T. F. Heinz, S. S. Hong, J. Huang, A. F. Ismach, E. Johnston-Halperin, M. Kuno, V. V Plashnitsa, R. D. Robinson, R. S. Ruoff, S. Salahuddin, J. Shan, L. Shi, M. G. Spencer, M. Terrones, W. Windl, and J. E. Goldberger, “Progress, challenges, and opportunities in two-dimensional materials beyond graphene,” *ACS Nano*, vol. 7, no. 4, pp. 2898–2926, 2013.

[27] F. Xia, D. B. Farmer, Y. M. Lin, and P. Avouris, “Graphene field-effect transistors with high on/off current ratio and large transport band gap at room temperature,” *Nano Lett.*, vol. 10, no. 2, pp. 715–718, 2010.

[28] B. Radisavljevic, A. Radenovic, J. Brivio, V. Giacometti, and A. Kis, “Single-layer MoS2 transistors,” *Nat. Nanotechnol.*, vol. 6, no. 3, pp. 147–150, 2011.

[29] X. Miao, S. Tongay, M. K. Petterson, K. Berke, A. G. Rinzler, B. R. Appleton, and A. F. Hebard, “High efficiency graphene solar cells by chemical doping,” *Nano Lett.*, vol. 12, no. 6, pp. 2745–2750, 2012.

[30] M. L. Tsai, S. H. Su, J. K. Chang, D. S. Tsai, C. H. Chen, C. I. Wu, L. J. Li, L. J. Chen, and J. H. He, “Monolayer MoS2 heterojunction solar cells,” *ACS Nano*, vol. 8, no. 8, pp. 8317–8322, 2014.

[31] T.-H. Han, Y. Lee, M.-R. Choi, S.-H. Woo, S.-H. Bae, B. H. Hong, J.-H. Ahn, and T.-W. Lee, “Extremely efficient flexible organic light-emitting diodes with modified graphene anode,” *Nat. Photonics*, vol. 6, no. 2, pp. 105–110, 2012.

[32] F. Schedin, A. K. Geim, S. V. Morozov, E. W. Hill, P. Blake, M. I. Katsnelson, and K. S. Novoselov, “Detection of individual gas molecules adsorbed on graphene,” *Nat. Mater.*, vol. 6, no. 9, pp. 652–655, 2007.

[33] C. Liu, Z. Yu, D. Neff, A. Zhamu, and B. Z. Jang, “Graphene-based supercapacitor with an ultrahigh energy density,” *Nano Lett.*, vol. 10, no. 12, pp. 4863–4868, 2010.

[34] C. A. Merchant, K. Healy, M. Wanunu, V. Ray, N. Peterman, J. Bartel, M. D. Fischbein, K. Venta, Z. Luo, A. T. C. Johnson, and M. Drndić, “DNA translocation through graphene nanopores,” *Nano Lett.*, vol. 10, no. 8, pp. 2915–2921, 2010.

[35] A. Castellanos-Gomez, V. Singh, H. S. J. Van Der Zant, and G. A. Steele, “Mechanics of freely-suspended ultrathin layered materials,” *Annalen der Physik*, vol. 527, no. 1–2. pp. 27–44, 2015.

[36] F. Wang, Y. Zhang, C. Tian, C. Girit, A. Zettl, M. Crommie, and Y. R. Shen, “Gate-Variable Optical Transitions in Graphene,” *Science (80-.).*, vol. 320, no. 5873, pp. 206–209, 2008.

[37] T.-H. Lee, S. Bhunia, and M. Mehregany, “Electromechanical Computing at 500 C with Silicon Carbide,” *Science (80-.).*, vol. 329, no. 5997, pp. 1316–1318, 2010.

[38] M. Bagheri, M. Poot, M. Li, W. P. H. Pernice, and H. X. Tang, “Dynamic manipulation of nanomechanical resonators in the high-amplitude regime and non-volatile mechanical memory operation,” *Nat. Nanotechnol.*, vol. 6, no. 11, pp. 726–732, 2011.

[39] C. Chen, “Graphene NanoElectroMechanical Resonators and Oscillators (PhD thesis),”

California Insitute of Technology, 2013.

[40] J. S. Bunch, A. M. van der Zande, S. S. Verbridge, I. W. Frank, D. M. Tanenbaum, J. M. Parpia, H. G. Craighead, and P. L. McEuen, "Electromechanical Resonators from Graphene Sheets," *Science (80-.).*, vol. 315, no. 5811, pp. 490–493, 2007.

[41] J. Lee, Z. Wang, K. He, J. Shan, and P. X. L. Feng, "High frequency MoS2 nanomechanical resonators," *ACS Nano*, vol. 7, no. 7, pp. 6086–6091, 2013.

[42] X. Q. Zheng, J. Lee, and P. X. L. Feng, "Hexagonal boron nitride (h-BN) nanomechanical resonators with temperature-dependent multimode operations," *2015 Transducers - 2015 18th Int. Conf. Solid-State Sensors, Actuators Microsystems, TRANSDUCERS 2015*, vol. 2, pp. 1393–1396, 2015.

[43] N. Rouhi, Y. Y. Wang, and P. J. Burke, "Ultrahigh conductivity of large area suspended few layer graphene films," *Appl. Phys. Lett.*, vol. 101, no. 26, 2012.

[44] A. M. Van Der Zande, R. A. Barton, J. S. Alden, C. S. Ruiz-Vargas, W. S. Whitney, P. H. Q. Pham, J. Park, J. M. Parpia, H. G. Craighead, and P. L. McEuen, "Large-scale arrays of single-layer graphene resonators," *Nano Lett.*, vol. 10, no. 12, pp. 4869–4873, 2010.

[45] H. Arjmandi-Tash, A. Allain, Z. (Vitto) Han, and V. Bouchiat, "Large scale integration of CVD-graphene based NEMS with narrow distribution of resonance parameters," *2D Mater.*, vol. 4, no. 2, p. 25023, 2017.

[46] F. Bonaccorso, A. Lombardo, T. Hasan, Z. Sun, L. Colombo, and A. C. Ferrari, "Production and processing of graphene and 2d crystals," *Mater. Today*, vol. 15, no. 12, pp. 564–589, 2012.

[47] I. S. I. Web, S. This, H. Press, M. Science, N. York, and A. Nw, "Graphene : Status and Prospects," vol. 1530, no. 2009, pp. 1530–1535, 2012.

[48] J. S. Bunch, S. S. Verbridge, J. S. Alden, A. M. Van Der Zande, J. M. Parpia, H. G. Craighead, and P. L. McEuen, "Impermeable atomic membranes from graphene sheets," *Nano Lett.*, vol. 8, no. 8, pp. 2458–2462, 2008.

[49] C. Chen, S. Rosenblatt, K. I. Bolotin, W. Kalb, P. Kim, I. Kymissis, H. L. Stormer, T. F. Heinz, and J. Hone, "Performance of monolayer graphene nanomechanical resonators with electrical readout," *Nat. Nanotechnol.*, vol. 4, no. 12, pp. 861–867, 2009.

[50] A. Eichler, J. Moser, J. Chaste, M. Zdrojek, I. Wilson-Rae, and A. Bachtold, "Nonlinear damping in mechanical resonators made from carbon nanotubes and graphene," *Nat. Nanotechnol.*, vol. 6, no. 6, pp. 339–342, 2011.

[51] S. Shivaraman, R. A. Barton, X. Yu, J. Alden, L. Herman, M. S. V Chandrashekhar, J.

Park, P. L. McEuen, J. M. Parpia, H. G. Craighead, and M. G. Spencer, “Free-standing epitaxial graphene,” *Nano Lett.*, vol. 9, no. 9, pp. 3100–3105, 2009.

[52] C. Chen and J. Hone, “Graphene nanoelectromechanical systems,” *Proc. IEEE*, vol. 101, no. 7, pp. 1766–1779, 2013.

[53] Y. Xu, C. Chen, V. V. Deshpande, F. A. Direnno, A. Gondarenko, D. B. Heinz, S. Liu, P. Kim, and J. Hone, “Radio frequency electrical transduction of graphene mechanical resonators,” *Appl. Phys. Lett.*, vol. 97, no. 24, 2010.

[54] M. Di Gisi, “2D Material-Based Bolometer,” École Polytechnique Fédérale de Lausanne, 2016.

[55] S. Bae, H. K. Kim, Y. Lee, X. Xu, J.-S. Park, Y. Zheng, J. Balakrishnan, D. Im, T. Lei, Y. Il Song, Y. J. Kim, K. S. Kim, B. Özyilmaz, J.-H. Ahn, B. H. Hong, and S. Iijima, “30 inch Roll-Based Production of High-Quality Graphene Films for Flexible Transparent Electrodes,” vol. 5, no. June, pp. 1–5, 2009.

[56] P. R. Whelan, B. S. Jessen, R. Wang, B. Luo, A. C. Stoot, D. M. A. Mackenzie, P. Braeuninger-Weimer, A. Jouvray, L. Prager, L. Camilli, S. Hofmann, P. B??ggild, and T. J. Booth, “Raman spectral indicators of catalyst decoupling for transfer of CVD grown 2D materials,” *Carbon N. Y.*, vol. 117, pp. 75–81, 2017.

[57] L. Gao, G.-X. Ni, Y. Liu, B. Liu, A. H. Castro Neto, and K. P. Loh, “Face-to-face transfer of wafer-scale graphene films,” *Nature*, vol. 505, no. 7482, pp. 190–194, 2013.

[58] X. Li, W. Cai, J. An, S. Kim, J. Nah, D. Yang, R. Piner, A. Velamakanni, I. Jung, E. Tutuc, S. K. Banerjee, L. Colombo, and R. S. Ruoff, “Large-Area Synthesis of High-Quality and Uniform Graphene Films on Copper Foils,” *Science (80-.).*, vol. 324, no. 5932, pp. 1312–1314, 2009.

[59] K. S. Kim, Y. Zhao, H. Jang, S. Y. Lee, J. M. Kim, K. S. Kim, J.-H. Ahn, P. Kim, J.-Y. Choi, and B. H. Hong, “Large-scale pattern growth of graphene films for stretchable transparent electrodes,” *Nature*, vol. 457, no. 7230, pp. 706–710, 2009.

[60] J. W. Suk, A. Kitt, C. W. Magnuson, Y. Hao, S. Ahmed, J. An, A. K. Swan, B. B. Goldberg, and R. S. Ruoff, “Transfer of CVD-grown monolayer graphene onto arbitrary substrates,” *ACS Nano*, vol. 5, no. 9, pp. 6916–6924, 2011.

[61] J.-Y. Hong and J. Jang, “Micropatterning of graphene sheets: recent advances in techniques and applications,” *J. Mater. Chem.*, vol. 22, no. 17, p. 8179, 2012.

[62] Y. Zhou and K. P. Loh, “Making patterns on graphene,” *Adv. Mater.*, vol. 22, no. 32, pp. 3615–3620, 2010.

[63] Y. Zhou, Q. Bao, B. Varghese, L. A. L. Tang, C. K. Tan, C. H. Sow, and K. P. Loh,

"Microstructuring of graphene oxide nanosheets using direct laser writing," *Adv. Mater.*, vol. 22, no. 1, pp. 67–71, 2010.

[64] K. Yong, A. Ashraf, P. Kang, and S. Nam, "Rapid Stencil Mask Fabrication Enabled One-Step Polymer-Free Graphene Patterning and Direct Transfer for Flexible Graphene Devices," *Sci. Rep.*, vol. 6, no. 1, p. 24890, 2016.

[65] X. Liang, Z. Fu, and S. Y. Chou, "Graphene transistors fabricated via transfer-printing in device active-areas on large wafer," *Nano Lett.*, vol. 7, no. 12, pp. 3840–3844, 2007.

[66] Z. Chen, Y. M. Lin, M. J. Rooks, and P. Avouris, "Graphene nano-ribbon electronics," *Phys. E Low-Dimensional Syst. Nanostructures*, vol. 40, no. 2, pp. 228–232, 2007.

[67] R. F. Pease, "Maskless lithography," in *Microelectronic Engineering*, 2005, vol. 78–79, no. 1–4, pp. 381–392.

[68] A. C. Ferrari, "Raman spectroscopy of graphene and graphite: Disorder, electron-phonon coupling, doping and nonadiabatic effects," *Solid State Commun.*, vol. 143, no. 1–2, pp. 47–57, 2007.

[69] M. Wall, "The Raman Spectroscopy of Graphene and the Determination of Layer Thickness," *Thermo Sci.*, p. 5, 2011.

[70] P. Blake, E. W. Hill, A. H. Castro Neto, K. S. Novoselov, D. Jiang, R. Yang, T. J. Booth, and A. K. Geim, "Making graphene visible," *Appl. Phys. Lett.*, vol. 91, no. 6, 2007.

[71] P. Y. Huang, C. S. Ruiz-Vargas, A. M. van der Zande, W. S. Whitney, M. P. Levendorf, J. W. Kevek, S. Garg, J. S. Alden, C. J. Hustedt, Y. Zhu, J. Park, P. L. McEuen, and D. A. Muller, "Grains and grain boundaries in single-layer graphene atomic patchwork quilts," *Nature*, vol. 469, no. 7330, pp. 389–392, 2011.

[72] C. Chen, S. Rosenblatt, K. I. Bolotin, W. Kalb, P. Kim, I. Kymissis, H. L. Stormer, T. F. Heinz, and J. Hone, "Performance of monolayer graphene nanomechanical resonators with electrical readout," *Nat. Nanotechnol.*, vol. 4, no. 12, pp. 861–867, 2009.

[73] Y. Nachshon, "Photoresist removal," *US Pat. 5,114,834*, 1992.

[74] M. Ishigami, J. H. Chen, W. G. Cullen, M. S. Fuhrer, and E. D. Williams, "Atomic structure of graphene on SiO2.," *Nano Lett.*, vol. 7, no. 6, pp. 1643–1648, 2007.

[75] J. Moser, A. Barreiro, and A. Bachtold, "Current-induced cleaning of graphene," *Appl. Phys. Lett.*, vol. 91, no. 16, pp. 4–6, 2007.

[76] Z. Moktadir, S. Boden, H. Mizuta, and H. Rutt, "Graphene for Nano-Electro-Mechanical Systems," *Nano Lett.*, vol. 3521, no. 2001, pp. 1–4, 2010.

[77] Y. Il Lee, K. H. Park, J. Lee, C. S. Lee, H. J. Yoo, C. J. Kim, and Y. S. Yoon, "Dry release for surface micromachining with HF vapor-phase etching," *J.*

Microelectromechanical Syst., vol. 6, no. 3, pp. 226–233, 1997.

[78] A. Goetzberger, R. M. Scarlett, and W. Shockley, "Research and Investigation of Inverse Epitaxial UHF Power Transistors," 1964.

[79] A. Venugopal, L. Colombo, and E. M. Vogel, "Contact resistance in few and multilayer graphene devices," *Appl. Phys. Lett.*, vol. 96, no. 1, 2010.

[80] J. S. Moon, M. Antcliffe, H. C. Seo, D. Curtis, S. Lin, A. Schmitz, I. Milosavljevic, A. A. Kiselev, R. S. Ross, D. K. Gaskill, P. M. Campbell, R. C. Fitch, K. M. Lee, and P. Asbeck, "Ultra-low resistance ohmic contacts in graphene field effect transistors," *Appl. Phys. Lett.*, vol. 100, no. 20, 2012.

[81] W. Li, Y. Liang, D. Yu, L. Peng, K. P. Pernstich, T. Shen, A. R. Hight Walker, G. Cheng, C. A. Hacker, C. A. Richter, Q. Li, D. J. Gundlach, and X. Liang, "Ultraviolet/ozone treatment to reduce metal-graphene contact resistance," *Appl. Phys. Lett.*, vol. 102, no. 18, 2013.

[82] B.-C. Huang, M. Zhang, Y. Wang, and J. Woo, "Contact resistance in top-gated graphene field-effect transistors," *Appl. Phys. Lett.*, vol. 99, no. 3, p. 32107, 2011.

[83] C. Liang, Y. Wang, and T. Li, "Studies on contact resistance in graphene based devices," *Microsyst. Technol.*, vol. 22, no. 8, pp. 1943–1947, 2016.

[84] I. N. Kholmanov, C. W. Magnuson, A. E. Aliev, H. Li, B. Zhang, J. W. Suk, L. L. Zhang, E. Peng, S. H. Mousavi, A. B. Khanikaev, R. Piner, G. Shvets, and R. S. Ruoff, "Improved electrical conductivity of graphene films integrated with metal nanowires," *Nano Lett.*, vol. 12, no. 11, pp. 5679–5683, 2012.

[85] K. I. Bolotin, K. J. Sikes, Z. Jiang, M. Klima, G. Fudenberg, J. Hone, P. Kim, and H. L. Stormer, "Ultrahigh electron mobility in suspended graphene," *Solid State Commun.*, vol. 146, no. 9–10, pp. 351–355, 2008.

[86] P. Blake, P. D. Brimicombe, R. R. Nair, T. J. Booth, D. Jiang, F. Schedin, L. A. Ponomarenko, S. V. Morozov, H. F. Gleeson, E. W. Hill, A. K. Geim, and K. S. Novoselov, "Graphene-based liquid crystal device," *Nano Lett.*, vol. 8, no. 6, pp. 1704–1708, 2008.

[87] X. Li, Y. Zhu, W. Cai, M. Borysiak, B. Han, D. Chen, R. D. Piner, L. Colomba, and R. S. Ruoff, "Transfer of large-area graphene films for high-performance transparent conductive electrodes," *Nano Lett.*, vol. 9, no. 12, pp. 4359–4363, 2009.

[88] X. Wang, J. Li, Q. Zhong, Y. Zhong, and M. Zhao, "Wafer-scale synthesis and transfer of monolayer graphene," in *Proceedings of the IEEE Conference on Nanotechnology*, 2013, pp. 652–655.

[89] C. N. Lau, W. Bao, and J. Velasco, “Properties of suspended graphene membranes,” *Materials Today*, vol. 15, no. 6. pp. 238–245, 2012.

[90] H. Park, I. Park, D. Yool, J. Park, D. Kim, J. Y. Woo, and J. Lee, “De-doping of graphene by Joule heating with water.”

[91] graphene.ac.rs, “Micromechanical Exfoliation.” [Online]. Available: http://www.graphene.ac.rs/graphene-main.html. [Accessed: 17-Jun-2017].

[92] N. Mishra, J. Boeckl, N. Motta, and F. Iacopi, “Graphene growth on silicon carbide: A review,” *Phys. Status Solidi*, vol. 213, no. 9, pp. 2277–2289, 2016.

[93] Minotlab.physics.oregonstate.edu, “Chemical vapour deposition of graphene on copper.” [Online]. Available: http://minotlab.physics.oregonstate.edu. [Accessed: 17-Jun-2017].

[94] G. Tuttle, “Contact resistance and TLM measurements.” pp. 1–11, 2014.